

## A massive rock and ice avalanche caused the 2021 disaster at Chamoli, Indian Himalaya

**Authors:** Shugar, D.H.<sup>1\*</sup>, Jacquemart, M.<sup>2,3,4</sup>, Shean, D.<sup>5</sup>, Bhushan, S.<sup>5</sup>, Upadhyay, K.<sup>6</sup>, Sattar, A.<sup>7</sup>, Schwanghart, W.<sup>8</sup>, McBride, S.<sup>9</sup>, Van Wyk de Vries, M.<sup>10,11</sup>, Mergili, M.<sup>12,13</sup>, Emmer, A.<sup>12</sup>, Deschamps-Berger, C.<sup>14</sup>, McDonnell, M.<sup>15</sup>, Bhambri, R.<sup>16</sup>, Allen, S.<sup>7,17</sup>, Berthier, E.<sup>18</sup>, Carrivick, J.L.<sup>19</sup>, Clague, J.J.<sup>20</sup>, Dokukin, M.<sup>21</sup>, Dunning, S.A.<sup>22</sup>, Frey, H.<sup>7</sup>, Gascoin, S.<sup>14</sup>, Haritashya, U.K.<sup>23</sup>, Huggel, C.<sup>7</sup>, Käb, A.<sup>24</sup>, Kargel, J.S.<sup>25</sup>, Kavanaugh, J.L.<sup>26</sup>, Lacroix, P.<sup>27</sup>, Petley, D.<sup>28</sup>, Rupper, S.<sup>15</sup>, Azam, M.F.<sup>29</sup>, Cook, S.J.<sup>30,31</sup>, Dimri, A.P.<sup>32</sup>, Eriksson, M.<sup>33</sup>, Farinotti, D.<sup>3,4</sup>, Fiddes, J.<sup>34</sup>, Gnyawali, K.R.<sup>35</sup>, Harrison, S.<sup>36</sup>, Jha, M.<sup>37</sup>, Koppes, M.<sup>38</sup>, Kumar, A.<sup>39</sup>, Leinss, S.<sup>40,41</sup>, Majeed, U.<sup>42</sup>, Mal, S.<sup>43</sup>, Muhuri, A.<sup>14,44</sup>, Noetzli, J.<sup>34</sup>, Paul, F.<sup>7</sup>, Rashid, I.<sup>42</sup>, Sain, K.<sup>39</sup>, Steiner, J.<sup>45,46</sup>, Ugalde, F.<sup>47,48</sup>, Watson, C.S.<sup>49</sup>, Westoby, M.J.<sup>50</sup>

### Affiliations:

<sup>1</sup>Water, Sediment, Hazards, and Earth-surface Dynamics (waterSHED) Lab, Department of Geoscience; University of Calgary, AB, Canada.

<sup>2</sup>Cooperative Institute for Research in Environmental Sciences, University of Colorado; Boulder, CO, USA.

<sup>3</sup>Laboratory of Hydraulics, Hydrology and Glaciology (VAW), ETH Zurich; Zurich, Switzerland.

<sup>4</sup>Swiss Federal Institute for Forest, Snow and Landscape Research WSL; Birmensdorf, Switzerland.

<sup>5</sup>Department of Civil and Environmental Engineering, University of Washington; Seattle, WA, USA.

<sup>6</sup>Independent journalist/water policy researcher; Nainital, Uttarakhand, India.

<sup>7</sup>Department of Geography, University of Zurich; Zurich, Switzerland.

<sup>8</sup>Institute of Environmental Science and Geography, University of Potsdam; Potsdam, Germany.

<sup>9</sup>U.S. Geological Survey, Earthquake Science Center; Moffett Field, CA, USA.

<sup>10</sup>Department of Earth & Environmental Sciences, University of Minnesota; Minneapolis, MN, USA.

<sup>11</sup>St. Anthony Falls Laboratory, University of Minnesota; Minneapolis, MN, USA.

<sup>12</sup>Institute of Geography and Regional Science, University of Graz; Graz, Austria.

<sup>13</sup>Institute of Applied Geology, University of Natural Resources and Life Sciences (BOKU); Vienna, Austria.

<sup>14</sup>CESBIO, Université de Toulouse, CNES/CNRS/IRD/UP; Toulouse, France.

<sup>15</sup>Department of Geography, University of Utah; Salt Lake City, Utah, USA.

<sup>16</sup>Department of Geography, South Asia Institute, Heidelberg University; Heidelberg, Germany.

<sup>17</sup>Institute for Environmental Sciences, University of Geneva; Switzerland.

<sup>18</sup>LEGOS, Université de Toulouse, CNES/CNRS/IRD/UPS; Toulouse, France.

<sup>19</sup>School of Geography and water@leeds, University of Leeds, Leeds; West Yorkshire, UK.

<sup>20</sup>Department of Earth Sciences, Simon Fraser University; Burnaby, BC, Canada.

<sup>21</sup>Department of Natural Disasters, High-Mountain Geophysical Institute; Nalchik, Russia.

<sup>22</sup>Geography, Politics and Sociology, Newcastle University; Newcastle, UK.

- <sup>23</sup>Department of Geology and Environmental Geosciences, University of Dayton; Dayton, OH, USA.
- <sup>24</sup>Department of Geosciences, University of Oslo; Oslo, Norway.
- <sup>25</sup>Planetary Science Institute; Tucson, AZ, USA.
- <sup>26</sup>Earth and Atmospheric Sciences, University of Alberta; Edmonton, AB, Canada.
- <sup>27</sup>ISTerre, Université Grenoble Alpes, IRD, CNRS; Grenoble, France.
- <sup>28</sup>Department of Geography, The University of Sheffield; Sheffield, UK.
- <sup>29</sup>Indian Institute of Technology Indore; India.
- <sup>30</sup>Geography and Environmental Science, University of Dundee; Dundee, UK.
- <sup>31</sup>UNESCO Centre for Water Law, Policy and Science, University of Dundee; Dundee, UK.
- <sup>32</sup>School of Environmental Sciences, Jawaharlal Nehru University; New Delhi, India.
- <sup>33</sup>Stockholm International Water Institute; Stockholm, Sweden.
- <sup>34</sup>WSL Institute for Snow and Avalanche Research SLF; Davos, Switzerland.
- <sup>35</sup>School of Engineering, University of British Columbia; Kelowna, BC, Canada.
- <sup>36</sup>College of Life and Environmental Sciences, University of Exeter, Penryn, UK.
- <sup>37</sup>Department of Mines and Geology, National Earthquake Monitoring and Research Center; Kathmandu, Nepal.
- <sup>38</sup>Department of Geography, University of British Columbia; Vancouver, BC, Canada.
- <sup>39</sup>Wadia Institute of Himalayan Geology, Dehradun; Uttarakhand, India.
- <sup>40</sup>Institute of Environmental Engineering (IfU), ETH Zurich, 8093 Zürich, Switzerland
- <sup>41</sup>Current affiliation: LISTIC, Université Savoie Mont Blanc, 74940 Annecy, France
- <sup>42</sup>Department of Geoinformatics, University of Kashmir; Hazratbal Srinagar, Jammu and Kashmir, India.
- <sup>43</sup>Department of Geography, Shaheed Bhagat Singh College, University of Delhi; Delhi, India.
- <sup>44</sup>Institute of Geography, Heidelberg University; Germany.
- <sup>45</sup>International Centre for Integrated Mountain Development; Kathmandu, Nepal.
- <sup>46</sup>Department of Physical Geography, Utrecht University; Netherlands.
- <sup>47</sup>Geoestudios, San José de Maipo; Chile.
- <sup>48</sup>Department of Geology, University of Chile; Santiago, Chile.
- <sup>49</sup>COMET, School of Earth and Environment. University of Leeds; Leeds, UK.
- <sup>50</sup>Department of Geography and Environmental Sciences, Northumbria University; Newcastle upon Tyne, UK.

\*Corresponding author. Email: daniel.shugar@ucalgary.ca



81 **Abstract:** On 7 Feb 2021, a catastrophic mass flow descended the Ronti Gad, Rishiganga, and  
82 Dhauliganga valleys in Chamoli, Uttarakhand, India, causing widespread devastation and  
83 severely damaging two hydropower projects. Over 200 people were killed or are missing. Our  
84 analysis of satellite imagery, seismic records, numerical model results, and eyewitness videos  
85 reveals that  $\sim 27 \times 10^6 \text{ m}^3$  of rock and glacier ice collapsed from the steep north face of Ronti  
86 Peak. The rock and ice avalanche rapidly transformed into an extraordinarily large and mobile  
87 debris flow that transported boulders  $> 20 \text{ m}$  in diameter, and scoured the valley walls up to 220  
88 m above the valley floor. The intersection of the hazard cascade with downvalley infrastructure  
89 resulted in a disaster, which highlights key questions about adequate monitoring and sustainable  
90 development in the Himalaya as well as other remote, high-mountain environments.

91  
92 **One-Sentence Summary:** The Chamoli disaster was triggered by an extraordinary rock and ice  
93 avalanche and debris flow, that destroyed infrastructure and left 204 people dead or missing.  
94

95 **Main Text:** Steep slopes, high topographic relief, and seismic activity make mountain regions  
96 prone to extremely destructive mass movements (e.g. 1). The sensitivity of glaciers and  
97 permafrost to climate changes is exacerbating these hazards (e.g. 2–7). Hazard cascades, where  
98 an initial event causes a downstream chain reaction (e.g. 8), can be particularly far-reaching,  
99 especially when they involve large amounts of water (7, 9, 10). An example is the 1970  
100 Huascarán avalanche, Peru, that was one of the largest, farthest-reaching, and deadliest ( $\sim 6000$   
101 lives lost) mass flows (11). Similarly, in 2013, over 4,000 people died at Kedarnath,  
102 Uttarakhand, India, when a moraine-dammed lake breached following heavy rainfall and  
103 snowmelt (12–14). Between 1894 and 2021, the Uttarakhand Himalaya has witnessed at least 16  
104 major disasters from flash floods, landslides, and earthquakes (14, 15).

105 Human activities that intersect with the mountain cryosphere can increase risk (16) and are  
106 common in Himalayan valleys where hydropower development is proliferating due to growing  
107 energy demands, the need for economic development, and efforts to transition into a low-carbon  
108 society (17, 18). Hydropower projects in Uttarakhand and elsewhere in the region have been  
109 opposed over their environmental effects, public safety, and issues associated with justice and  
110 rehabilitation (19, 20).

111 On 7 Feb 2021, a massive rock and ice avalanche from the 6063 m-high Ronti Peak generated a  
112 cascade of events that caused more than 200 deaths or missing persons, as well as damage or  
113 destruction of infrastructure that most notably included two hydropower projects in the  
114 Rishiganga and Dhauliganga valleys (Fig. 1, table S1) (21). Here, we present a rapid and  
115 comprehensive reconstruction of the hazard cascade. We leveraged multiple types of remote  
116 sensing data, eyewitness videos, numerical modeling, seismic data, and reconnaissance field  
117 observations in a collaborative, global effort to understand this event. We also describe the  
118 antecedent conditions and the immediate societal response, allowing us to consider some wider  
119 implications for sustainable development in high-mountain environments.

## 120 **February 7 2021 hazard cascade**

121 At 4:51 UTC (10:21 Indian Standard Time [IST]), about  $26.9 \times 10^6 \text{ m}^3$  (95% confidence interval:  
122  $26.5\text{--}27.3 \times 10^6 \text{ m}^3$ ) of rock and ice (Fig. 1, 2) detached from the steep north face of Ronti Peak at  
123 an elevation of about 5,500 m asl, and impacted the Ronti Gad ('gad' means rivulet) valley floor

about 1,800 m below. We estimated the onset of this avalanche and its velocity by analyzing seismic data from two distant stations, 160 and 174 km southeast of the source (Fig. S6) (22, §5.1). The initial failure happened between 4:51:13 and 4:51:21 UTC, based on a source-sensor wave travel-time correction. We attributed a high-frequency signal 55 to 58 seconds later to the impact of the avalanche on the valley bottom, indicating a mean speed of the rock and ice avalanche of between 57 and 60 ms<sup>-1</sup> (205 to 216 km h<sup>-1</sup>) down the ~35° steep mountain face.

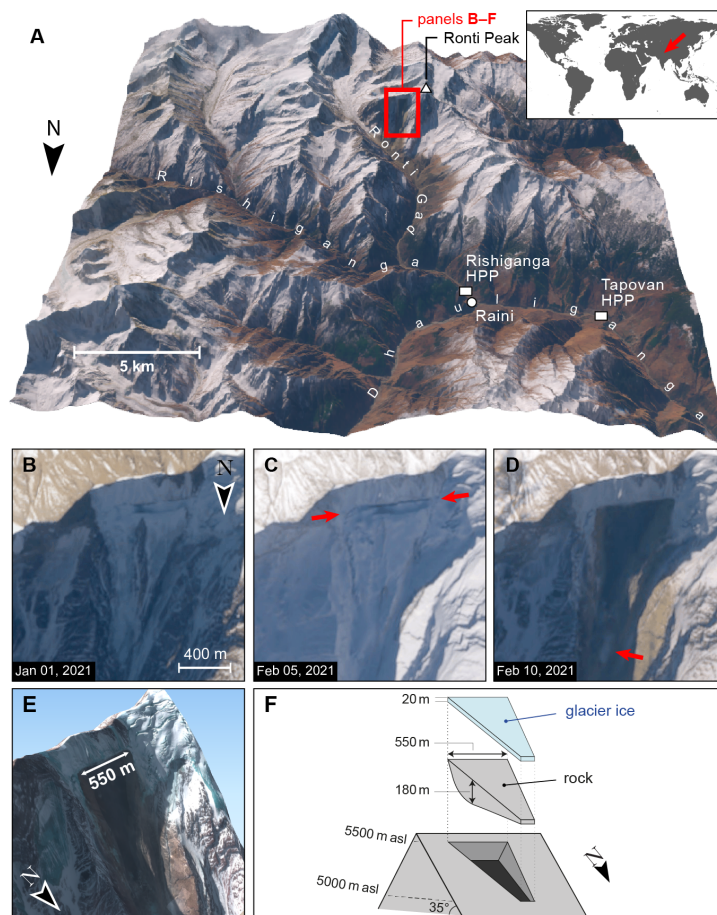


**Fig. 1. Overview of the Chamoli disaster, Uttarakhand, India.** (A) 3D rendering of the local geography, with labels for main place names mentioned in the text. HPP stands for hydropower project. (B-D) Pre- and post-event satellite imagery of the site of the collapsed rock and glacier block, and the resulting scar. Note snow cover in the region just before the event (C). The red arrows in (C) mark the fracture that became the headscarp of the landslide (22, §3.2 and fig. S4).

138 The arrow in D points to a remaining part of the lower eastern glacier. (E) 3D rendering of the  
139 scar. (F) Schematic of failed mass of rock and ice. Satellite imagery in (A–D) and (E) is from  
140 Sentinel-2 (Copernicus Sentinel Data 02-10-2021) and Pléiades-HR (© CNES 02-10-2021,  
141 Distribution AIRBUS DS), respectively.

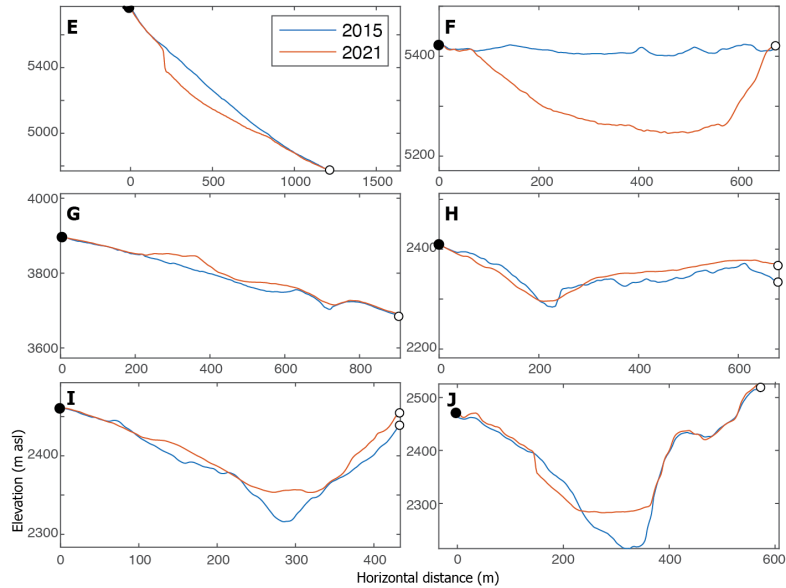
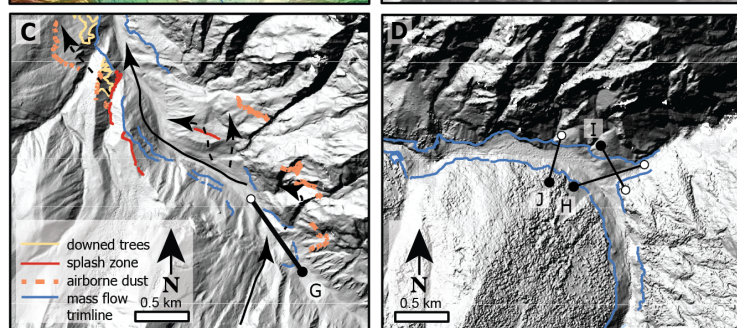
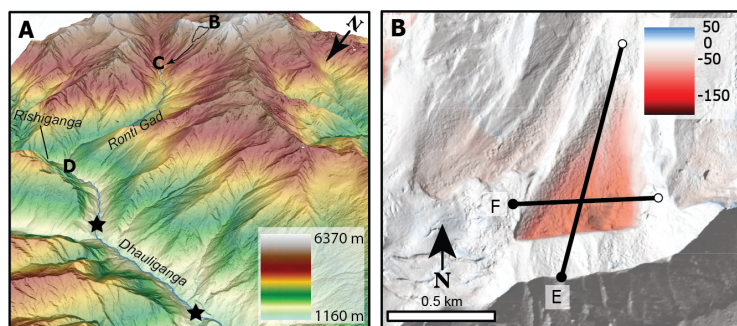


**Fig. 2. Satellite-derived elevation data of the Chamoli hazard cascade.** (A) Perspective view of the area, from the landslide source at Ronti Peak to the Rishiganga and Tapovan Vishnugad hydropower projects (black stars). (B) Elevation change over the landslide scar based on DEM-differencing between September 2015 and February 10-11, 2021. (C) The proximal valley floor, with geomorphic interpretations of the flow path. (D) Confluence of Ronti Gad and Rishiganga River. (E-J) Topographic profiles showing elevation change due to rock/icefall and sediment deposition for locations shown in (B-D). Elevation loss on the inner bank in (J) is primarily due to the destruction of forest.

Differencing of high-resolution digital elevation models (DEMs) revealed a failure scar that has a vertical difference of up to 180 m and a slope-normal thickness of ~80 m on average, and a slab width up to ~550 m, including both bedrock and overlying glacier ice (Fig. 2). The lowermost part of the larger eastern glacier is still in place and was not eroded by the rock and ice avalanche moving over it (Fig. 1D), suggesting that the avalanche may have become airborne for a short period during its initial descent. Optical feature tracking detected movement of the failed rock block as early as 2016, with the largest displacement in the summer months of 2017 and 2018 (fig. S4). This movement opened a fracture up to 80 m wide in the glacier and into the underlying bedrock (Fig. 1, fig. S5). Geodetic analysis and glacier thickness inversions indicate that the collapsed mass comprised ~80% rock and ~20% glacier ice by volume (22, §5.2, fig. S10). Melt of this ice was essential to the downstream evolution of the flow, as water transformed the rock and ice avalanche into a highly mobile debris flow (cf. 23, 24). Media reports (25) suggest that some ice blocks (diameter <1 m) were found in tunnels at the Tapovan Vishnugad hydropower site (hereafter referred to as the Tapovan project), and some videos of the debris flow (22, §5.3) show floating blocks that we interpret as ice, indicating that some of the ice survived at considerable distance downstream. Notably, and in contrast to most previously documented rock avalanches, very little debris is preserved at the base of the failed slope. This is likely due to the large volumes of water (22, §5.5) that resulted in a high mobility of the flow.

Geomorphic mapping based on very high-resolution satellite images (Table S2) acquired during and immediately after the event, provides evidence of the flow evolution. We detected four components of the catastrophic mass flow, beginning with the main rock and ice avalanche from Ronti Peak described above (component one).

The second component is “splash deposits” (cf. 26–28), which are relatively fine-grained, wet sediments that became airborne as the mass flow ran up adjacent slopes. For example, the rock and ice avalanche traveled up a steep slope on the east side of the valley opposite the source zone, and some material became airborne, being deposited at a height of about 120 m above the valley floor. These deposits include boulders up to ~8 m (a-axis length). The bulk of the flow then traveled back to the proximal (west) side of the valley and rode up a ridge ~220 m above the valley floor, before becoming airborne and splashing into a smaller valley to the west (Fig. 2C, figs. S15, S18). Boulders up to 13 m (a-axis length) were deposited near the top of the ridge. Vegetation remained intact on the lee side of some ridges that were overrun by the splashing mass.

A third component of the mass flow is reflected in airborne dust deposition. A dust cloud is visible in PlanetScope imagery from 5:01 UTC and 5:28 UTC February 7 (10:31 and 10:58 IST). A smooth layer of debris, estimated from satellite imagery to be only a few cm in thickness, was deposited higher than the splash deposits, up to ~500 m above the valley floor, although the boundary between the airborne dust deposition and other mass flow deposits is indistinct in places. Signs of the largely airborne splash and dust components can be observed over ~3.5 km downstream of the valley impact site. The avalanche also generated a powerful air blast (cf. *I*) that flattened about 0.2 km<sup>2</sup> of forest on the west side of the Ronti Gad valley (Fig. 2C).

After the rock and ice avalanche impacted the valley floor, most of it moved downvalley in a northwesterly direction. Frictional heating of the ice in the avalanche generated liquid water that allowed the transition in flow characteristics, becoming more fluid downvalley, creating a flow consisting of sediment, water, and blocks of ice. The uppermost part of the valley floor deposits is around 0.75 x10<sup>6</sup> m<sup>3</sup>, with remarkably few large boulders that typically form the upper surface of rock avalanches (e.g. 29, 30) (Fig. 2G, fig. S16). The mass flow traveled downvalley and superelevated (runup elevation) up to ~130 m above the valley floor around bends (fig. S17). Clear trimlines, at some places at multiple levels, are evident along much of the flow path (e.g. Fig. 2C, D).

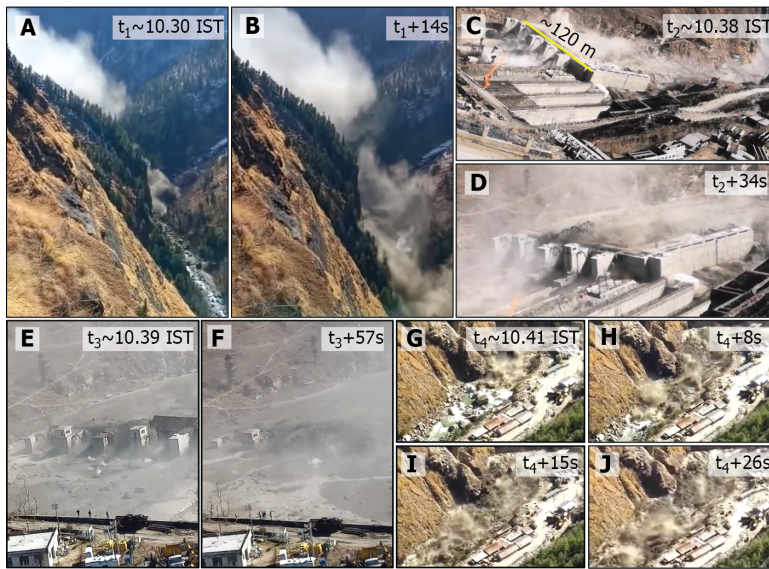
At the confluence of the Ronti Gad and Rishiganga River, a ~40 m thick deposit of debris blocked the Rishiganga valley (Fig. 2H, I). Deposition in this area probably resulted from deceleration of the mass flow at a sharp turn to the west. During the days following the event, a lake ~700 m long formed behind these deposits in the Rishiganga valley upstream of its confluence with Ronti Gad. The lake was still present two months later and had grown since the initial formation. Substantial deposition occurred about 1 km downstream of the confluence, where material up to ~100 m thick was deposited on the valley floor (Fig. 2J). DEM differencing shows that the total deposit volume at the Ronti Gad-Rishiganga River confluence and just downstream was ~8x10<sup>6</sup> m<sup>3</sup>. These large sediment deposits likely indicate the location where the flow transitioned to a debris flow (*3I*) - the fourth component.

A field reconnaissance by co-authors from the Wadia Institute of Himalayan Geology indicates that the impact of debris flow material (sediment, water, ice, woody debris) at the confluence of Rishiganga River with Dhauliganga River created a bottleneck and forced some material 150-200 m up the Dhauliganga (fig. S15). The release of the water a few minutes later led to the destruction of a temple on the north bank of the Dhauliganga.

A substantial fraction of the fine-grained material involved in the event was transported far downstream. This more dilute flow could be considered a fifth component. Approximately 24 hours after the initial landslide, the sediment plume was visible in PlanetScope and Sentinel-2 imagery in the hydropower project's reservoir on the Alaknanda River at Srinagar, about 150 km downstream from the source. About 2½ weeks later, increased turbidity was observed at Kanpur on the Ganges River, ~900 km from the source. An official of the Delhi water quality board reported that 8 days after the Chamoli disaster, a chief water source for the city - a canal drawing directly from the Ganga River - had an unprecedented spike in suspended sediment (turbidity) 80 times the permissible level (*32*). The amount of corresponding sedimentation in

hydropower reservoirs and rivers is unknown, but possibly substantial, and may contribute to increased erosion on turbine blades, and infilling of reservoirs in the years to come.

Analysis of eyewitness videos permitted estimation of the propagation of the flow front below the Ronti Gad-Rishiganga River confluence (Fig. 3, 22, §5.3). The maximum frontal velocity reconstructed from these videos is  $\sim 25 \text{ m s}^{-1}$  near the Rishiganga hydropower project (fig. S11, table S5), which is about 15 km downstream of the rock and ice avalanche source. Just upstream of the Tapovan project (another  $\sim 10 \text{ km}$  downriver), the velocity decreased to  $\sim 16 \text{ m s}^{-1}$ , and just downstream of Tapovan (26 km from source), the velocity was  $\sim 12 \text{ m s}^{-1}$ . The large reduction in frontal velocity is likely related to impoundment behind the Tapovan project dam. Analysis of PlanetScope images (at 5:01 UTC and 5:28 UTC) suggests that the average frontal velocity between Raini (at Rishiganga hydropower project) and Joshimath (16 km downstream) was  $\sim 10 \text{ m s}^{-1}$ . We also estimated mean discharge from the videos to be between  $\sim 8,200$  and  $\sim 14,200 \text{ m}^3 \text{ s}^{-1}$  at the Rishiganga hydropower project and between  $\sim 2,900$  and  $\sim 4,900 \text{ m}^3 \text{ s}^{-1}$  downstream of the Tapovan project. Estimates for the debris flow duration are complicated by uncertain volumes, water contents, discharge amounts, and shapes of discharge curves at specific locations. For Rishiganga, for example, we estimate a duration of 10-20 minutes, a number that appears realistic from the information available.



Parts a-b: Electricity Market in India: Dhauriganga 4\*70 MW Coffor Dam collapse in Uttarakhand Chamoli... Prayers for Uttarakhand; URL: <https://www.youtube.com/watch?v=96nopaNn-Qp4&t=1s>, accessed: 28th February 2021  
Parts c-d: Kamlesh Malikhan; (<https://www.facebook.com/100005762340793/videos/1678161685719227/> (since removed)); Permission: verbal permission of the author given to Kavita Upadhyay  
Parts e-f: Manvar Rawat (<https://www.facebook.com/100007108448247/videos/2796749477238640/>); Permission: verbal permission of the author given to Kavita Upadhyay  
Parts g-j: RW • Rshikeshwritings: Uttarakhand Flood 2021[] Rshikesh , Srinagar , Devprayag , Haridwar, URL: <https://www.youtube.com/watch?v=QEDlPLgubY>, accessed: 28th February

**Fig. 3. Sample video frames used to analyse flood velocity and discharge.** (A,B) Flow front arrives and rushes through the valley upstream of the Rishiganga project (location P1 in Fig. 4). (C) Flow front arrives at Tapovan project's dam (location P3). (D) The reservoir is being filled quickly; spillways are damaged. (E) The dam is overtopped. (F) Collapse of

remaining structures. **(G-J)** Flow front proceeds down the valley below the Tapovan dam (location P4); spreading into the village in (J).

We conducted numerical simulations with *r.avaflow* (22, §5.4), which indicate that the rock and ice avalanche could not have transitioned to the debris flow seen farther downstream without an accompanying reduction in the debris volume. If such a direct transition had occurred, the modeling suggests that the flow discharge would be approximately one order of magnitude higher than the estimates derived from video recordings (22, §5.4). The deposition patterns we observed in satellite imagery support the hypothesis that the vicinity of the Ronti Gad-Rishiganga River confluence played a key role in flow transition. Our numerical simulations are consistent with the escape of a fluid-rich front from the rock and ice avalanche mass near this confluence (Fig. 4A), reproducing mapped trimlines and estimated flow velocities and discharges down to Tapovan (Fig. 4B, C). Our simulated discharge estimates at P1–P4 are within the ranges derived from the video analysis (Fig. 4D, 22, §5.3), and simulated travel times between P0–P3 (Fig. 4D) show excellent agreement (<5% difference) with travel times inferred from seismic data, videos, and satellite imagery. We found less agreement between the numerical model results and the reconstructions from videos farther downstream due to the complex effects of the Tapovan project in slowing the flow, which are at a finer scale than is represented by our model.



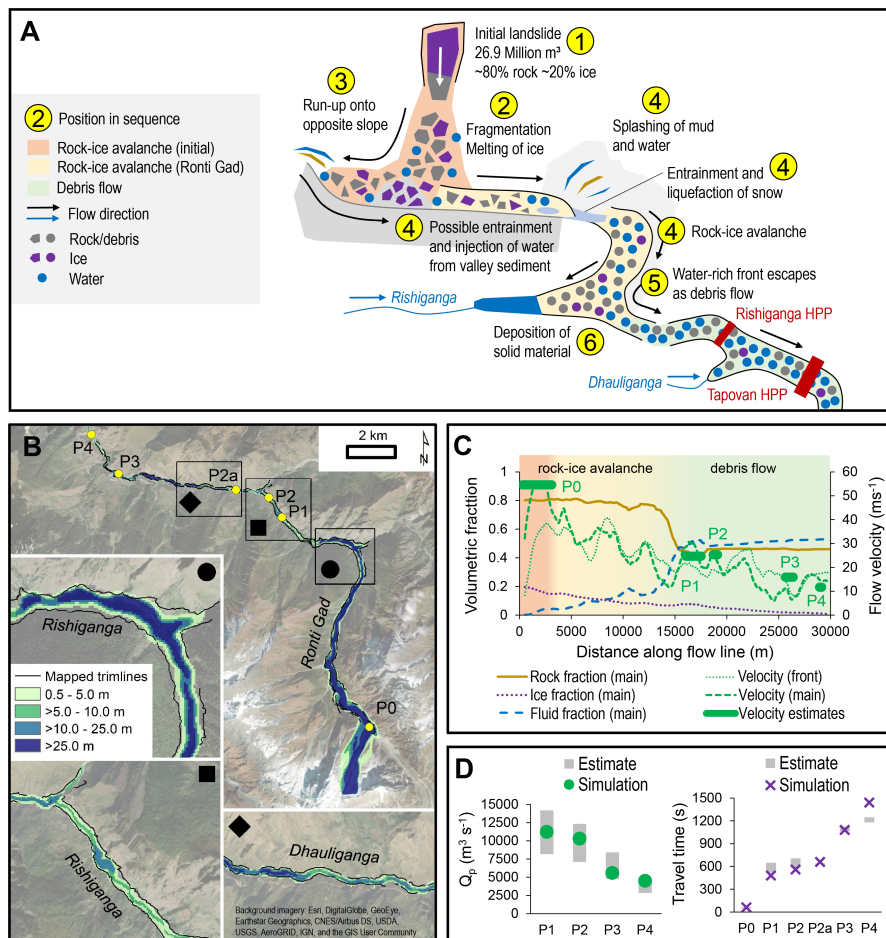


**Fig. 4. Flow evolution scenarios and simulation. (A)** Schematic of the evolution of the flow from the source to Tapovan. **(B)** Maximum flow height simulated with r.avaflo, showing the observed trim lines for comparison. P0 is the location of the velocity estimate derived from seismic data, P1-P4 are locations of velocity estimates based on videos and satellite images. **(C)** Along-profile evolution of flow velocity and fractions of rock/debris, ice, and water simulated with r.avaflo. **(D)** Simulated and estimated peak discharges and travel times at above locations. In the legend labels, (front) refers to the flow front whereas (main) refers to the point of maximum flow momentum.

## Causes and implications

The February 7 rock and ice avalanche was a very large event with an extraordinarily high fall height that resulted in a disaster due to its extreme mobility and the presence of downstream infrastructure. The ~3700 m vertical drop to the Tapovan HPP is surpassed clearly by only two known events in the historic record, namely the 1962 and 1970 Huascaran avalanches (11), while its mobility ( $H/L = 0.16$  at Tapovan, where  $H$  is fall height and  $L$  is flow length) is exceeded only by a few recent glacier detachments (10). The location of the failure was due to the extremely steep and high relief of Ronti Peak. The sheared nature of the source rocks and contrasting interbedded rock types likely conditioned the failure (22, §1). The large and expanding fracture (Fig 1B, C) at the head scarp may have allowed liquid water to penetrate into the bedrock, increasing pore-water pressures or enhancing freeze-thaw weathering.

Nearly all (190) of the 204 people either killed or missing in the disaster (22, §2, Table S1) were workers at the Rishiganga (13.2 MW) and Tapovan (520 MW) project sites (33). Direct economic losses from damage to the two hydropower structures alone are over 223 million USD (34, 35). The high loss of human life and infrastructure damage was due to the debris flow, and not the initial rock and ice avalanche. However, not all large, high-mountain rock and ice avalanches transform into highly mobile debris flows that cause destruction far from their source (9).

Our energy balance estimates indicate that most of the  $\sim 5\text{--}6 \times 10^6 \text{ m}^3$  volume of glacier ice first warmed (along with a portion of the rock mass) from approximately  $-8^\circ\text{C}$  to  $0^\circ\text{C}$  and then melted through frictional heating during the avalanche as it descended to the Rishiganga valley, involving a drop of approximately 3400 m (22, §5.5). Potential other sources of water were considered, including glacier lake outburst floods, catastrophic drainage of water from reservoirs such as surface lakes, ice deposited by earlier avalanches, and enlithic reservoirs. No evidence for such sources was observed in available remote sensing data. A slow-moving storm system moved through the area in the days before Feb 7. We estimate that a  $\sim 220,000\text{--}360,000 \text{ m}^3$  contribution from precipitation over the Ronti Gad basin was a minor component of the flow, representing only 4–7% of the water equivalent contained in the initial glacier ice detachment. Similarly, while water already present in the river, water ejected from groundwater, melting snow, wet sediment, and water released from the run-of-the-river hydroelectric project may have all contributed to the debris flow, even when taken together (with generous error margins), these sum to a small amount compared to the probable range of water volumes in the mass movement. The major effect of ice melt on the mobility of rock and ice avalanches is documented (9, 10), but it appears that the combination of the specific rock/ice fraction ( $\sim 80/20\%$  by volume) and large fall height of the rock and ice avalanche led to a rare, severe event during which nearly all of the ice melted.

Soon after the disaster, media reports and expert opinions started to circulate, postulating links of the event to climate change. Recent attribution studies demonstrated that glacier mass loss on global, regional and local scales is to a large extent attributable to anthropogenic greenhouse gas forcing (36, 37). High-mountain slope failures in rock and ice, however, pose additional challenges to attribution due to multiple factors and processes involved in such events. While long-term trends of increasing slope failure occurrence in some regions

could be attributed to climate change (16, 38, 39), attribution of single events such as the Chamoli event remains largely elusive. Nevertheless, certain elements of the Chamoli event have potential links to climate, and weather, as described below. Furthermore, the Chamoli event may be seen in the context of a change in geomorphological sensitivity (40) and might therefore be seen as a precursor for an increase in such events as climate warming proceeds.

The stability of glacierized and perennially frozen high-mountain slopes is indeed particularly sensitive to climate change (16). Our analysis suggests regional climate and related cryospheric change could have interacted in a complex way with the geologic and topographic setting to produce this massive slope failure. Air and surface temperatures have been increasing across the Himalayan region, with greater rates of warming during the second half of the 20th Century and at higher elevations (41, 42). Most glaciers in the Himalaya are shrinking and mass loss rates are accelerating across the region (22, §1, 43–46). Glacier shrinkage uncovers and destabilizes mountain flanks and strongly alters the hydrological and thermal regimes of the underlying rock.

The detachment zone at Ronti Peak is about 1 km higher than the regional lower limit of permafrost at around 4,000 to 4,500 m asl., as indicated by rock glaciers in the region and global permafrost maps (47, 48). Exposed rock on the north face of Ronti Peak likely contains cold permafrost with rock temperatures several degrees below 0°C. In connection with glaciers, however, ground temperatures can be locally higher. The ice-free south face of Ronti Peak is certainly substantially warmer with rock temperatures perhaps around or above 0°C, causing strong south-to-north lateral heat fluxes (49). Permafrost temperatures are increasing worldwide, in particular in cold permafrost (16, 50, 51), leading to long-term and deep-seated thermal anomalies, and even permafrost degradation (49). Increasing ground temperatures at the failure site of the Chamoli avalanche could have resulted in reduced strength of the frozen rock mass by altering the rock hydrology and the mechanical properties of discontinuities and the failed rock mass (52).

The geology of the failed rocks includes several observed or inferred critical attributes (22, §1): (i) The rocks are cut by multiple directions of planar weaknesses; the failed mass detached along four of these. (ii) The rock mass is close to a major thrust fault, with many local shear fractures, which - along with other discontinuities - would have facilitated aqueous chemical weathering. (iii) The rock types (schist and gneiss), even when nominally unweathered, contain abundant soft, platy, oriented, and geomechanically anisotropic minerals (phyllosilicates and kyanite especially); Weathering will further weaken these rocks, and they will be more likely to disintegrate into fine material upon impact, which would influence the rheology and likely enhance the mobility of the mass flow.

Importantly, the 7 Feb failure considerably changed the stress regime and thermal conditions in the area of the detachment zone. Only detailed investigations and monitoring will determine whether rock or ice adjacent to the failed block (including a large hanging rock block above the scarp) were destabilized due to these changes and present an ongoing hazard. Similarly, the impoundment at the Ronti Gad-Rishiganga River confluence requires careful monitoring as embedded ice in the dam deposits may melt with warmer temperatures,

increasing the risk of an outburst flood by reducing lake freeboard of the dam, and/or reducing structural coherence of the dam.

Videos of the event, including the ones broadcast on social media in real time (22, §5.3), showed that the people directly at risk had little to no warning. This leads us to question what could have happened if a warning system had been installed. We estimate that a suitably designed early warning system might have allowed for 6 to 10 minutes of warning before the arrival of the debris flow at the Tapovan project (perhaps up to 20 minutes if situated near the landslide source, or if a dense seismic network was leveraged (53)), which may have provided enough time to evacuate at least some workers from the power project. After the event, a new flood warning system was installed near Raini (22, §2.1, fig. S15D). Studies show that early warning system design and installation is technically feasible but rapid communication of reliable warnings and appropriate responses by individuals to alerts, are complex (54). Previous research indicates that effective early warning requires public education, including drills, which would increase awareness of potential hazards and improve ability to take action when disaster strikes (55, 56). Considering the repeated failures from the same slope in the past two decades (22, §1), public education and drills in the Chamoli region would be very beneficial.

## Conclusions

On the morning of 7 Feb 2021, a large rock and ice avalanche descended the Ronti Gad valley, rapidly transforming into a highly mobile debris flow that destroyed two hydropower plants and left more than 200 people dead or missing. We identified three primary drivers for the severity of the Chamoli disaster: (1) the extraordinary fall height, providing ample gravitational potential energy; (2) the worst-case rock:ice ratio, which resulted in almost complete melting of the glacier ice, enhancing the mobility of the debris flow; and (3) the unfortunate location of multiple hydropower plants in the direct path of the flow.

The debris flow disaster started as a wedge failure sourced in bedrock near the crest of Ronti Peak, and included an overlying hanging glacier. The rock almost completely disintegrated in the ~1 minute that the wedge took to fall (~5500 – 3,700 m asl), and the rock:ice ratio of the detached mass was almost exactly the critical value required for near-complete melting of the ice. As well as having a previous history of large mass movements, the mountain is riven with planes and points of structural weakness, and further bedrock failures as well as large ice and snow avalanches are inevitable.

Videos of the disaster were rapidly distributed through social media, attracting widespread international media coverage and catalyzing an immediate response from the international scientific community. This response effort quickly leveraged images from modern commercial and civilian government satellite constellations that offer exceptional resolution, "always-on" cadence, rapid tasking, and global coverage. This event demonstrated that if appropriate human resources and technologies are in place, post-disaster analysis can be reduced to days or hours. Nevertheless, ground-based evidence remains crucial for clarifying the nature of such disasters.

Although we cannot attribute this individual disaster specifically to climate change, the possibly increasing frequency of high-mountain slope instabilities can likely be related to observed atmospheric warming and corresponding long-term changes in cryospheric conditions (glaciers, permafrost). Multiple factors beyond those listed above contributed to the Chamoli rock and ice avalanche, including the geologic structure and steep topography, possible long-term thermal disturbances in permafrost bedrock induced by atmospheric warming, stress changes due to the decline and collapse of adjacent and overlying glaciers, and enhanced melt water infiltration during warm periods.

The Chamoli event also raises important questions about clean energy development, climate change adaptation, disaster governance, conservation, environmental justice, and sustainable development in the Himalaya and other high-mountain environments. This stresses the importance of a better understanding of the cause and impact of mountain hazards, leading to disasters. While the scientific aspects of this event are the focus of our study, we cannot ignore the human suffering and emerging socio-economic impacts that it caused. It was the human tragedy that motivated the authors to examine available data and explore how these data, analyses, and interpretations can be used to help inform decision-making at the ground level.

The disaster tragically revealed the risks associated with the rapid expansion of hydropower infrastructure into increasingly unstable territory. Enhancing inclusive dialogues among governments, local stakeholders and communities, private sector, and the scientific community could help assess, minimize, and prepare for existing risks. The disaster indicates that the long-term sustainability of planned hydroelectric power projects must account for both current and future social and environmental conditions, while mitigating risks to infrastructure, personnel, and downstream communities. Conservation values carry elevated weight in development policies and infrastructure investments where the needs for social and economic development interfere with areas prone to natural hazards, putting communities at risk.

## References

1. J. S. Kargel, G. J. Leonard, D. H. Shugar, U. K. Haritashya, A. Bevington, E. J. Fielding, K. Fujita, M. Geertsema, E. S. Miles, J. Steiner, E. Anderson, S. Bajracharya, G. W. Bawden, D. F. Breashears, A. Byers, B. Collins, M. R. Dhital, A. Donnellan, T. L. Evans, M. L. Geai, M. T. Glasscoe, D. Green, D. R. Gurung, R. Heijenk, A. Hilborn, K. Hudnut, C. Huyck, W. W. Immerzeel, J. Liming, R. Jibson, A. Kääb, N. R. Khanal, D. Kirschbaum, P. D. A. Kraaijenbrink, D. Lamsal, L. Shiyin, L. Mingyang, D. McKinney, N. K. Nahirnick, N. Zhuotong, S. Ojha, J. Olsenholler, T. H. Painter, M. Pleasants, K. C. Pratima, Q. I. Yuan, B. H. Raup, D. Regmi, D. R. Rounce, A. Sakai, S. Donghui, J. M. Shea, A. B. Shrestha, A. Shukla, D. Stumm, M. van der Kooij, K. Voss, W. Xin, B. Weihs, D. Wolfe, W. Lizong, Y. Xiaojun, M. R. Yoder, N. Young, Geomorphic and geologic controls of geohazards induced by Nepal's 2015 Gorkha earthquake. *Science*. **351**, 140 (2016).

- 461 2. S. Allen, S. Cox, I. Owens, Rock avalanches and other landslides in the central Southern  
462 Alps of New Zealand: a regional study considering possible climate change impacts.  
463 *Landslides*. **8**, 33–48 (2011).
- 464 3. L. Fischer, R. S. Purves, C. Huggel, J. Noetzli, W. Haeberli, On the influence of  
465 topographic, geological and cryospheric factors on rock avalanches and rockfalls in high-  
466 mountain areas. *Natural Hazards and Earth System Sciences*. **12**, 241–254 (2012).
- 467 4. S. Gruber, R. Fleiner, E. Guegan, P. Panday, M.-O. Schmid, D. Stumm, P. Wester, Y.  
468 Zhang, L. Zhao, Review article: Inferring permafrost and permafrost thaw in the  
469 mountains of the Hindu Kush Himalaya region. *The Cryosphere*. **11**, 81–99 (2017).
- 470 5. A. Kääb, S. Leinss, A. Gilbert, Y. Bühler, S. Gascoin, S. G. Evans, P. Bartelt, E.  
471 Berthier, F. Brun, W.-A. Chao, D. Farinotti, F. Gimbert, W. Guo, C. Huggel, J. S.  
472 Kargel, G. J. Leonard, L. Tian, D. Treichler, T. Yao, Massive collapse of two glaciers in  
473 western Tibet in 2016 after surge-like instability. *Nature Geoscience*. **11**, 114–120  
474 (2018).
- 475 6. M. Jacquemart, M. Loso, M. Leopold, E. Welty, E. Berthier, J. S. S. Hansen, J. Sykes, K.  
476 Tiampo, What drives large-scale glacier detachments? Insights from Flat Creek glacier,  
477 St. Elias Mountains, Alaska. *Geology*. **48**, 703–707 (2020).
- 478 7. S. G. Evans, K. B. Delaney, N. M. Rana, in *Snow and Ice-Related Hazards, Risks, and*  
479 *Disasters (Second Edition)*, W. Haeberli, C. Whiteman, Eds. (Elsevier, 2021;  
480 <https://www.sciencedirect.com/science/article/pii/B9780128171295000044>), pp. 541–  
481 596.
- 482 8. D. Kirschbaum, C. S. Watson, D. R. Rounce, D. H. Shugar, J. S. Kargel, U. K.  
483 Haritashya, P. Amatya, D. E. Shean, E. R. Anderson, M. Jo, The state of remote sensing  
484 capabilities of cascading hazards over High Mountain Asia. *Frontiers in Earth Science*.  
485 **7** (2019), doi:10.3389/feart.2019.00197.
- 486 9. D. Schneider, C. Huggel, W. Haeberli, R. Kaitna, Unraveling driving factors for large  
487 rock-ice avalanche mobility. *Earth Surface Processes and Landforms*. **36**, 1948–1966  
488 (2011).
- 489 10. A. Kääb, M. Jacquemart, A. Gilbert, S. Leinss, L. Girod, C. Huggel, D. Falaschi, F.  
490 Ugalde, D. Petrakov, S. Chernomorets, M. Dokukin, F. Paul, S. Gascoin, E. Berthier, J.  
491 Kargel, Sudden large-volume detachments of low-angle mountain glaciers - more  
492 frequent than thought. *The Cryosphere*. **15**, 1751–1785 (2021).
- 493 11. S. G. Evans, N. F. Bishop, L. Fidel Smoll, P. Valderrama Murillo, K. B. Delaney, A.  
494 Oliver-Smith, A re-examination of the mechanism and human impact of catastrophic  
495 mass flows originating on Nevado Huascarán, Cordillera Blanca, Peru in 1962 and 1970.  
496 *Engineering Geology*. **108**, 96–118 (2009).

- 497 12. K. Upadhyay, A year later, no lessons learnt. *The Hindu* (2014), (available at  
498 [https://www.thehindu.com/opinion/op-ed/a-year-later-no-lessons-](https://www.thehindu.com/opinion/op-ed/a-year-later-no-lessons-learnt/article6120397.ece)  
499 [learnt/article6120397.ece](https://www.thehindu.com/opinion/op-ed/a-year-later-no-lessons-learnt/article6120397.ece)).
- 500 13. S. K. Allen, P. Rastner, M. Arora, C. Huggel, M. Stoffel, Lake outburst and debris flow  
501 disaster at Kedarnath, June 2013: hydrometeorological triggering and topographic  
502 predisposition. *Landslides*. **13**, 1479–1491 (2016).
- 503 14. R. Bhambri, M. Mehta, D. P. Dobhal, A. K. Gupta, B. Pratap, K. Kesarwani, A. Verma,  
504 Devastation in the Kedarnath (Mandakini) Valley, Garhwal Himalaya, during 16–17  
505 June 2013: a remote sensing and ground-based assessment. *Natural Hazards*. **80**, 1801–  
506 1822 (2016).
- 507 15. PIB, Statement in Parliament by Union Home Minister Shri Amit Shah regarding  
508 avalanche in the upper catchment of Rishiganga River in Chamoli District of  
509 Uttarakhand. *Press Information Bureau (PIB)* (2021), (available at  
510 <https://pib.gov.in/PressReleaseIframePage.aspx?PRID=1696552>).
- 511 16. R. Hock, G. Rasul, C. Adler, S. Caceres, S. Gruber, Y. Hirabayashi, M. Jackson, A.  
512 Kääb, S. Kang, S. Kutuzov, A. Milner, U. Molau, S. Morin, B. Orlove, H. Steltzer,  
513 “Chapter 2: High Mountain Areas — Special Report on the Ocean and Cryosphere in a  
514 Changing Climate,” *IPCC Special Report on the Ocean and Cryosphere in a Changing*  
515 *Climate* (2019), (available at <https://www.ipcc.ch/srocc/chapter/chapter-2/>).
- 516 17. K. S. Valdiya, Damming rivers in the tectonically resurgent Uttarakhand Himalaya.  
517 *Current Science*. **106**, 1658–1668 (2014).
- 518 18. R. A. Vaidya, D. J. Molden, A. B. Shrestha, N. Wagle, C. Tortajada, The role of  
519 hydropower in South Asia’s energy future. *International Journal of Water Resources*  
520 *Development*. **37**, 367–391 (2021).
- 521 19. A. Diduck, J. Sinclair, D. Pratap, G. Hostetler, Achieving meaningful public  
522 participation in the environmental assessment of hydro development: case studies from  
523 Chamoli District, Uttarakhand, India. *Impact Assessment and Project Appraisal*. **25**,  
524 219–231 (2007).
- 525 20. Kundan Singh v State of Uttarakhand, *High Court of Uttarakhand, India* (2019), vol.  
526 Writ Petition (P.I.L) No. 48 of 2019.
- 527 21. A. Shrestha, J. Steiner, S. Nepal, S. B. Maharjan, M. Jackson, G. Rasul, B. Bajracharya,  
528 Understanding the Chamoli flood: Cause, process, impacts, and context of rapid  
529 infrastructure development, (available at [https://www.icimod.org/article/understanding-](https://www.icimod.org/article/understanding-the-chamoli-flood-cause-process-impacts-and-context-of-rapid-infrastructure-development/)  
530 [the-chamoli-flood-cause-process-impacts-and-context-of-rapid-infrastructure-](https://www.icimod.org/article/understanding-the-chamoli-flood-cause-process-impacts-and-context-of-rapid-infrastructure-development/)  
531 [development/](https://www.icimod.org/article/understanding-the-chamoli-flood-cause-process-impacts-and-context-of-rapid-infrastructure-development/)).
- 532 22. Materials and methods are available as supplementary materials on Science Online.

- 533 23. W. Haeberli, C. Huggel, A. Kääb, S. Zraggen-Oswald, A. Polkvoj, I. Galushkin, I.  
534 Zotikov, N. Osokin, The Kolka-Karmadon rock/ice slide of 20 September 2002: an  
535 extraordinary event of historical dimensions in North Ossetia, Russian Caucasus.  
536 *Journal of Glaciology*. **50**, 533–546 (2004).
- 537 24. F. Walter, F. Amann, A. Kos, R. Kenner, M. Phillips, A. de Preux, M. Huss, C.  
538 Tognacca, J. Clinton, T. Diehl, Y. Bonanomi, Direct observations of a three million  
539 cubic meter rock-slope collapse with almost immediate initiation of ensuing debris  
540 flows. *Geomorphology*. **351**, 106933 (2020).
- 541 25. J. Koshy, Scientists studying samples to know roots of Uttarakhand glacier disaster. *The*  
542 *Hindu* (2021), (available at [https://www.thehindu.com/sci-tech/science/scientists-](https://www.thehindu.com/sci-tech/science/scientists-studying-samples-to-know-roots-of-uttarakhand-glacier-disaster/article33851727.ece)  
543 [studying-samples-to-know-roots-of-uttarakhand-glacier-disaster/article33851727.ece](https://www.thehindu.com/sci-tech/science/scientists-studying-samples-to-know-roots-of-uttarakhand-glacier-disaster/article33851727.ece)).
- 544 26. R. G. McConnell, R. W. Brock, “Report on the Great Landslide at Frank, Alta. 1903,”  
545 *Annual Report, Part VIII* (Department of the Interior Dominion of Canada, Ottawa,  
546 1904), p. 17.
- 547 27. J. F. Orwin, J. J. Clague, R. F. Gerath, The Cheam rock avalanche, Fraser Valley, British  
548 Columbia, Canada. *Landslides*. **1**, 289–298 (2004).
- 549 28. A. Mitchell, S. McDougall, J. Aaron, M.-A. Brideau, Rock avalanche-generated  
550 sediment mass flows: definitions and hazard. *Front. Earth Sci.* **8**, 543937 (2020).
- 551 29. S. A. Dunning, The grain-size distribution of rock-avalanche deposits in valley confined  
552 settings. *Italian Journal of Engineering Geology and Environment*. **1**, 117–121 (2006).
- 553 30. D. H. Shugar, J. J. Clague, The sedimentology and geomorphology of rock avalanche  
554 deposits on glaciers. *Sedimentology*. **58**, 1762–1783 (2011).
- 555 31. M. Church, M. Jakob, What Is a Debris Flood? *Water Resources Research*. **56** (2020),  
556 doi:10.1029/2020WR027144.
- 557 32. Hindustan Times, Water supply back to normal, says Delhi Jal Board after Chamoli  
558 impact. *Hindustan Times* (2021), (available at  
559 [https://www.hindustantimes.com/cities/others/normal-water-supply-to-resume-today-](https://www.hindustantimes.com/cities/others/normal-water-supply-to-resume-today-says-delhi-jal-board-101613412411000.html)  
560 [says-delhi-jal-board-101613412411000.html](https://www.hindustantimes.com/cities/others/normal-water-supply-to-resume-today-says-delhi-jal-board-101613412411000.html)).
- 561 33. Uttarakhand Emergency Operations Centre, “Daily Report (A.T.R.:39)” (Dehradun,  
562 2021).
- 563 34. S. Dutta, Fate of NTPC’s Tapovan project hangs in balance after Rs 1,500 crore loss.  
564 *The Economic Times* (2021), (available at  
565 [https://economictimes.indiatimes.com/industry/energy/power/fate-of-ntpcs-tapovan-](https://economictimes.indiatimes.com/industry/energy/power/fate-of-ntpcs-tapovan-project-hangs-in-balance-after-rs-1500-crore-loss/articleshow/80760066.cms)  
566 [project-hangs-in-balance-after-rs-1500-crore-loss/articleshow/80760066.cms](https://economictimes.indiatimes.com/industry/energy/power/fate-of-ntpcs-tapovan-project-hangs-in-balance-after-rs-1500-crore-loss/articleshow/80760066.cms)).



35. J. Mazoomdaar, Behind hydel project washed away, a troubled trail to accident in 2011. *The Indian Express* (2021), (available at <https://indianexpress.com/article/india/hydel-power-project-uttarakhand-flash-flood-glacier-burst-chamoli-district-7183561/>).
36. R. F. Stuart-Smith, G. H. Roe, S. Li, M. R. Allen, Increased outburst flood hazard from Lake Palcacocha due to human-induced glacier retreat. *Nature Geoscience*. **14**, 85–90 (2021).
37. G. H. Roe, J. E. Christian, B. Marzeion, On the attribution of industrial-era glacier mass loss to anthropogenic climate change. *The Cryosphere*. **15**, 1889–1905 (2021).
38. W. Cramer, M. Auffhammer, C. Hugel, U. Molau, M. A. F. S. Dias, A. Solow, D. A. Stone, L. Tibig, in *Climate Change 2014: Impacts, Adaptation, and Vulnerability. Part A: Global and Sectoral Aspects. Contribution of Working Group II to the Fifth Assessment Report of the Intergovernmental Panel on Climate Change*, C. B. Field, V. R. Barros, D. J. Dokken, K. J. Mach, M. D. Mastrandrea, T. E. Bilir, M. Chatterjee, K. L. Ebi, Y. O. Estrada, R. C. Genova, B. Girma, E. S. Kissel, A. N. Levy, S. MacCracken, P. R. Mastrandrea, L. L. White, Eds. (Cambridge University Press, Cambridge, UK, 2014), pp. 979–1337.
39. E. K. Bessette-Kirton, J. A. Coe, A 36-year record of rock avalanches in the Saint Elias Mountains of Alaska, with implications for future hazards. *Frontiers in Earth Science*. **8**, 293 (2020).
40. J. Knight, S. Harrison, The impacts of climate change on terrestrial Earth surface systems. *Nature Climate Change*. **3**, 24–29 (2013).
41. N. Pepin, R. S. Bradley, H. F. Diaz, M. Baraer, E. B. Caceres, N. Forsythe, H. Fowler, G. Greenwood, M. Z. Hashmi, X. D. Liu, J. R. Miller, L. Ning, A. Ohmura, E. Palazzi, I. Rangwala, W. Schöner, I. Severskiy, M. Shahgedanova, M. B. Wang, S. N. Williamson, D. Q. Yang, Mountain Research Initiative EDW Working Group, Elevation-dependent warming in mountain regions of the world. *Nature Climate Change*. **5**, 424–430 (2015).
42. T. P. Sabin, R. Krishnan, R. Vellore, P. Priya, H. P. Borgaonkar, B. B. Singh, A. Sagar, in *Assessment of Climate Change over the Indian Region: A Report of the Ministry of Earth Sciences (MoES), Government of India*, R. Krishnan, J. Sanjay, C. Gnanaseelan, M. Mujumdar, A. Kulkarni, S. Chakraborty, Eds. (Springer, Singapore, 2020; [https://doi.org/10.1007/978-981-15-4327-2\\_11](https://doi.org/10.1007/978-981-15-4327-2_11)), pp. 207–222.
43. M. F. Azam, P. Wagnon, E. Berthier, C. Vincent, K. Fujita, J. S. Kargel, Review of the status and mass changes of Himalayan-Karakoram glaciers. *Journal of Glaciology*. **64**, 61–74 (2018).
44. J. M. Maurer, J. M. Schaefer, S. Rupper, A. Corley, Acceleration of ice loss across the Himalayas over the past 40 years. *Science Advances*. **5**, eaav7266 (2019).

- 603 45. D. E. Shean, S. Bhushan, P. Montesano, D. R. Rounce, A. Arendt, B. Osmanoglu, A  
604 systematic, regional assessment of High Mountain Asia glacier mass balance. *Front.*  
605 *Earth Sci.* **7** (2020), doi:10.3389/feart.2019.00363.
- 606 46. R. Hugonnet, R. McNabb, E. Berthier, B. Menounos, C. Nuth, L. Girod, D. Farinotti, M.  
607 Huss, I. Dussaillant, F. Brun, A. Kääb, Accelerated global glacier mass loss in the early  
608 twenty-first century. *Nature*. **592**, 726–731 (2021).
- 609 47. S. Gruber, Derivation and analysis of a high-resolution estimate of global permafrost  
610 zonation. *The Cryosphere*. **6**, 221–233 (2012).
- 611 48. S. K. Allen, J. Fiddes, A. Linsbauer, S. S. Randhawa, B. Saklani, N. Salzmann,  
612 Permafrost Studies in Kullu District, Himachal Pradesh. *Current Science*. **111**, 550  
613 (2016).
- 614 49. J. Noetzli, S. Gruber, Transient thermal effects in Alpine permafrost. *The Cryosphere*. **3**,  
615 85–99 (2009).
- 616 50. B. K. Biskaborn, S. L. Smith, J. Noetzli, H. Matthes, G. Vieira, D. A. Streletskiy, P.  
617 Schoeneich, V. E. Romanovsky, A. G. Lewkowicz, A. Abramov, M. Allard, J. Boike, W.  
618 L. Cable, H. H. Christiansen, R. Delaloye, B. Diekmann, D. Drozdov, B. Etzel Müller, G.  
619 Grosse, M. Guglielmin, T. Ingeman-Nielsen, K. Isaksen, M. Ishikawa, M. Johansson, H.  
620 Johansson, A. Joo, D. Kaverin, A. Kholodov, P. Konstantinov, T. Kröger, C. Lambiel,  
621 J.-P. Lanckman, D. Luo, G. Malkova, I. Meiklejohn, N. Moskalenko, M. Oliva, M.  
622 Phillips, M. Ramos, A. B. K. Sannel, D. Sergeev, C. Seybold, P. Skryabin, A. Vasiliev,  
623 Q. Wu, K. Yoshikawa, M. Zheleznyak, H. Lantuit, Permafrost is warming at a global  
624 scale. *Nature Communications*. **10**, 264 (2019).
- 625 51. J. Noetzli, H. H. Christiansen, K. Isaksen, S. Smith, L. Zhao, D. A. Streletskiy,  
626 Permafrost thermal state. *Bulletin of the American Meteorological Society*. **101**, S34–S36  
627 (2020).
- 628 52. S. Gruber, W. Haeberli, Permafrost in steep bedrock slopes and its temperature-related  
629 destabilization following climate change. *Journal of Geophysical Research - Earth*  
630 *Surface*. **112** (2007), doi:10.1029/2006JF000547.
- 631 53. N. P. Rao, R. Rekapalli, D. Srinagesh, V. M. Tiwari, N. Hovius, K. L. Cook, M. Dietze,  
632 Seismological rockslide warnings in the Himalaya. *Science*. **372**, 247–247 (2021).
- 633 54. I. Kelman, M. H. Glantz, in *Reducing Disaster: Early Warning Systems For Climate*  
634 *Change* (Springer Netherlands, Dordrecht, 2014; [http://link.springer.com/10.1007/978-](http://link.springer.com/10.1007/978-94-017-8598-3_5)  
635 [94-017-8598-3\\_5](http://link.springer.com/10.1007/978-94-017-8598-3_5)), pp. 89–108.
- 636 55. S. K. McBride, A. Bostrom, J. Sutton, R. M. de Groot, A. S. Baltay, B. Terbush, P.  
637 Bodin, M. Dixon, E. Holland, R. Arba, P. Laustsen, S. Liu, M. Vinci, Developing post-  
638 alert messaging for ShakeAlert, the earthquake early warning system for the West Coast  
639 of the United States of America. *International Journal of Disaster Risk Reduction*. **50**,  
640 101713–101713 (2020).

- 641 56. W. Pollock, J. Wartman, Human vulnerability to landslides. *GeoHealth*. **4** (2020),  
642 doi:10.1029/2020GH000287.
- 643 57. Sentinel Hub, (available at <https://www.sentinel-hub.com/>).
- 644 58. PlanetLabs, Education and Research - Satellite Imagery Solutions. *Planet* (2021),  
645 (available at <https://planet.com/markets/education-and-research/>).
- 646 59. Maxar, Uttarakhand Flooding, (available at [https://www.maxar.com/open-](https://www.maxar.com/open-data/uttarakhand-flooding)  
647 [data/uttarakhand-flooding](https://www.maxar.com/open-data/uttarakhand-flooding)).
- 648 60. S. Bhushan, D. Shean, Chamoli Disaster Pre-event 2-m DEM Composite: September  
649 2015 (Version 1.0) [Data set] (2021), (available at <https://zenodo.org/record/4554647>).
- 650 61. D. Shean, S. Bhushan, E. Berthier, C. Deschamps-Berger, S. Gascoin, F. Knuth, Chamoli  
651 Disaster Post-event 2-m DEM Composite (February 10-11, 2021) and Difference Map  
652 (v1.0) [Data set] (2021), (available at <https://zenodo.org/record/4558692>).
- 653 62. r.avaflow | The mass flow simulation tool, (available at <https://www.avaflow.org/>).
- 654 63. R. K. Maikhuri, U. Rana, K. S. Rao, S. Nautiyal, K. G. Saxena, Promoting ecotourism in  
655 the buffer zone areas of Nanda Devi Biosphere Reserve: An option to resolve people—  
656 policy conflict. *International Journal of Sustainable Development & World Ecology*. **7**,  
657 333–342 (2000).
- 658 64. P. K. Mukherjee, A. K. Jain, S. Singhal, N. B. Singha, S. Singh, K. Kumud, P. Seth, R.  
659 C. Patel, U-Pb zircon ages and Sm-Nd isotopic characteristics of the Lesser and Great  
660 Himalayan sequences, Uttarakhand Himalaya, and their regional tectonic implications.  
661 *Gondwana Research*. **75**, 282–297 (2019).
- 662 65. C. Montemagni, C. Montomoli, S. Iaccarino, R. Carosi, A. K. Jain, H.-J. Massonne, I. M.  
663 Villa, Dating protracted fault activities: microstructures, microchemistry and  
664 geochronology of the Vaikrita Thrust, Main Central Thrust zone, Garhwal Himalaya,  
665 NW India. *Geological Society, London, Special Publications*. **481**, 127–146 (2019).
- 666 66. K. S. Valdiya, O. P. Goel, Lithological subdivision and petrology of the Great  
667 Himalayan Vaikrita Group in Kumaun, India. *Proc. Indian Acad. Sci. (Earth Planet*  
668 *Sci.)*. **92**, 141–163 (1983).
- 669 67. N. I. Norrish, D. C. Wyllie, in *Landslides: Investigation and Mitigation* (Transportation  
670 Research Board Special Report, 1996; <https://trid.trb.org/view/462513>), pp. 391–425.
- 671 68. T. K. Raghuvanshi, Plane failure in rock slopes – A review on stability analysis  
672 techniques. *Journal of King Saud University - Science*. **31**, 101–109 (2019).
- 673 69. R. C. Patel, V. Adlakha, P. Singh, Y. Kumar, N. Lal, Geology, structural and exhumation  
674 history of the Higher Himalayan Crystallines in Kumaon Himalaya, India. *Journal of the*  
675 *Geological Society of India*. **77**, 47–72 (2011).

- 676 70. J. Célérier, T. M. Harrison, A. A. G. Webb, A. Yin, The Kumaun and Garwhal Lesser  
677 Himalaya, India: Part 1. structure and stratigraphy. *GSA Bulletin*. **121**, 1262–1280  
678 (2009).
- 679 71. W. Xu, R. Bürgmann, Z. Li, An improved geodetic source model for the 1999 Mw 6.3  
680 Chamoli earthquake, India. *Geophysical Journal International*. **205**, 236–242 (2016).
- 681 72. S. G. Evans, G. Scarascia-Mugnozza, A. L. Strom, R. L. Hermanns, A. Ischuk, S.  
682 Vinnichenko, in *Landslides from Massive Rock Slope Failure; NATO Science Series: IV,*  
683 *Earth and Environmental Sciences*, S. G. Evans, G. Scarascia-Mugnozza, A. L. Strom,  
684 R. L. Hermanns, Eds. (Springer, Dordrecht, 2006), pp. 3–52.
- 685 73. J. Fiddes, S. Gruber, TopoSCALE v.1.0: downscaling gridded climate data in complex  
686 terrain. *Geoscientific Model Development*. **7**, 387–405 (2014).
- 687 74. R. Bhambri, T. Bolch, R. K. Chaujar, S. C. Kulshreshtha, Glacier changes in the  
688 Garhwal Himalaya, India, from 1968 to 2006 based on remote sensing. *Journal of*  
689 *Glaciology*. **57**, 543–556 (2011).
- 690 75. V. Kumar, T. Shukla, M. Mehta, D. P. Dobhal, M. P. Singh Bisht, S. Nautiyal, Glacier  
691 changes and associated climate drivers for the last three decades, Nanda Devi region,  
692 Central Himalaya, India. *Quaternary International*. **575–576**, 213–226 (2021).
- 693 76. A. Banerjee, A. P. Dimri, K. Kumar, Temperature over the Himalayan foothill state of  
694 Uttarakhand: Present and future. *Journal of Earth System Science*. **130**, 33 (2021).
- 695 77. F. Brun, E. Berthier, P. Wagnon, A. Kaab, D. Treichler, A spatially resolved estimate of  
696 High Mountain Asia glacier mass balances from 2000 to 2016. *Nature Geoscience*. **10**,  
697 668–673 (2017).
- 698 78. J. Obu, S. Westermann, A. Bartsch, N. Berdnikov, H. H. Christiansen, A. Dashtseren, R.  
699 Delaloye, B. Elberling, B. Etzelmüller, A. Kholodov, A. Khomutov, A. Kääb, M. O.  
700 Leibman, A. G. Lewkowicz, S. K. Panda, V. Romanovsky, R. G. Way, A. Westergaard-  
701 Nielsen, T. Wu, J. Yamkhin, D. Zou, Northern Hemisphere permafrost map based on  
702 TTOP modelling for 2000–2016 at 1 km<sup>2</sup> scale. *Earth-Science Reviews*. **193**, 299–316  
703 (2019).
- 704 79. NTPC Limited, NTPC works on modalities for release of compensation; Rescue  
705 operation continues in full swing. *NTPC Limited* (2021), (available at  
706 [https://www.ntpc.co.in/en/media/press-releases/details/ntpc-works-modalities-release-](https://www.ntpc.co.in/en/media/press-releases/details/ntpc-works-modalities-release-compensation-rescue-operation-continues-full-swing)  
707 [compensation-rescue-operation-continues-full-swing](https://www.ntpc.co.in/en/media/press-releases/details/ntpc-works-modalities-release-compensation-rescue-operation-continues-full-swing)).
- 708 80. N. Santoshi, Uttarakhand disaster: Reni gets 1st warning system in case of sudden water  
709 surge. *Hindustan Times* (2021), (available at [https://www.hindustantimes.com/india-](https://www.hindustantimes.com/india-news/uttarakhand-disaster-reni-gets-1st-warning-system-in-case-of-sudden-water-surge-101613557801245.html#:~:text=Reni%2C the most-affected village,the village to recover bodies)  
710 [news/uttarakhand-disaster-reni-gets-1st-warning-system-in-case-of-sudden-water-surge-](https://www.hindustantimes.com/india-news/uttarakhand-disaster-reni-gets-1st-warning-system-in-case-of-sudden-water-surge-101613557801245.html#:~:text=Reni%2C the most-affected village,the village to recover bodies)  
711 [101613557801245.html#:~:text=Reni%2C the most-affected village,the village to](https://www.hindustantimes.com/india-news/uttarakhand-disaster-reni-gets-1st-warning-system-in-case-of-sudden-water-surge-101613557801245.html#:~:text=Reni%2C the most-affected village,the village to recover bodies)  
712 [recover bodies](https://www.hindustantimes.com/india-news/uttarakhand-disaster-reni-gets-1st-warning-system-in-case-of-sudden-water-surge-101613557801245.html#:~:text=Reni%2C the most-affected village,the village to recover bodies)).

- 713 81. W. Schwanghart, R. Worni, C. Huggel, M. Stoffel, O. Korup, Uncertainty in the  
714 Himalayan energy–water nexus: estimating regional exposure to glacial lake outburst  
715 floods. *Environmental Research Letters*. **11**, 074005 (2016).
- 716 82. W. Schwanghart, M. Ryan, O. Korup, Topographic and seismic constraints on the  
717 vulnerability of Himalayan hydropower. *Geophysical Research Letters*. **45**, 8985–8992  
718 (2018).
- 719 83. H. Regan, S. Gupta, Famous for its tree huggers, village at center of India glacier  
720 collapse warned of impending disaster for decades. No one listened. *CNN* (2021),  
721 (available at [https://edition.cnn.com/2021/02/12/asia/india-glacier-raini-village-chipko-](https://edition.cnn.com/2021/02/12/asia/india-glacier-raini-village-chipko-intl-hnk/index.html)  
722 [intl-hnk/index.html](https://edition.cnn.com/2021/02/12/asia/india-glacier-raini-village-chipko-intl-hnk/index.html)).
- 723 84. R. Guha, *The unquiet woods: ecological change and peasant resistance in the Himalaya*  
724 (Oxford University Press, New Delhi, 1989).
- 725 85. S. Pathak, *The Chipko Movement: A People's History* (Permanent Black, New Delhi,  
726 2021).
- 727 86. R. J. Wasson, N. Juyal, M. Jaiswal, M. McCulloch, M. M. Sarin, V. Jain, P. Srivastava,  
728 A. K. Singhvi, The mountain-lowland debate: Deforestation and sediment transport in  
729 the upper Ganga catchment. *Journal of Environmental Management*. **88**, 53–61 (2008).
- 730 87. M. Mashal, H. Kumar, Before Himalayan Flood, India Ignored Warnings of  
731 Development Risks. *The New York Times* (2021), (available at  
732 <https://www.nytimes.com/2021/02/08/world/asia/india-flood-ignored-warnings.html>).
- 733 88. K. Upadhyay, Dams and damages. *The Hindu* (2021), (available at  
734 <https://www.thehindu.com/opinion/op-ed/dams-and-damages/article33795426.ece>).
- 735 89. Expert Body Report, “Assessment of Environmental Degradation and Impact of  
736 Hydroelectric projects during the June 2013 Disaster in Uttarakhand.” (New Delhi,  
737 2014), (available at <http://gbpihedenvi.nic.in/PDFs/Disaster>  
738 [Data/Reports/Assessment\\_of\\_Environmental\\_Degradation.pdf](http://gbpihedenvi.nic.in/PDFs/Disaster)).
- 739 90. M. P. S. Bisht, P. Rautela, Disaster looms large over Joshimath. *Current Science*. **98**,  
740 1271–1271 (2010).
- 741 91. Standing Committee on Energy, “43rd Report” (New Delhi, 2019), (available at  
742 [http://164.100.47.193/isscommittee/Energy/16\\_Energy\\_43.pdf](http://164.100.47.193/isscommittee/Energy/16_Energy_43.pdf)).
- 743 92. SANDRP, Tapovan Vishnugad HPP: delays, damages and destructions. *South Asia*  
744 *Network on Dams, Rivers and People (SANDRP)* (2021), (available at  
745 <https://sandrp.in/2021/02/20/tapovan-vishnugad-hpp-delays-damages-and-destructions/>).
- 746 93. J. Grönwall, “Large dams and human rights obligations: The case of the Pancheshwar  
747 Multipurpose Project on the border between India and Nepal” (9789188495181,

- 748 Stockholm, 2020), (available at [https://www.siwi.org/wp-](https://www.siwi.org/wp-content/uploads/2020/07/Report_ICWC_HRBA_2020_WEB.pdf)  
749 [content/uploads/2020/07/Report\\_ICWC\\_HRBA\\_2020\\_WEB.pdf](https://www.siwi.org/wp-content/uploads/2020/07/Report_ICWC_HRBA_2020_WEB.pdf)).
- 750 94. K. D. Morell, M. Sandiford, C. P. Rajendran, K. Rajendran, A. Alimanovic, D. Fink, J.  
751 Sanwal, Geomorphology reveals active décollement geometry in the central Himalayan  
752 seismic gap. *Lithosphere*. **7**, 247–256 (2015).
- 753 95. R. E. S. Moss, E. M. Thompson, D. Scott Kieffer, B. Tiwari, Y. M. A. Hashash, I.  
754 Acharya, B. R. Adhikari, D. Asimaki, K. B. Clahan, B. D. Collins, S. Dahal, R. W.  
755 Jibson, D. Khadka, A. Macdonald, C. L. M. Madugo, H. Benjamin Mason, M. Pehlivan,  
756 D. Rayamajhi, S. Uprety, Geotechnical effects of the 2015 Magnitude 7.8 Gorkha,  
757 Nepal, earthquake and aftershocks. *Seismological Research Letters*. **86**, 1514–1523  
758 (2015).
- 759 96. S. P. Sati, S. Sharma, N. Rana, H. Dobhal, N. Juyal, Environmental implications of  
760 Pancheshwar dam in Uttarakhand (Central Himalaya), India. *Current Science*. **116**,  
761 1483–1489 (2019).
- 762 97. Alaknanda Hydro Power Co. Ltd. v Anuj Joshi & Others, *Supreme Court of India. Civil*  
763 *Appeal No. 6736 of 2013*. (2013).
- 764 98. Alaknanda Hydro Power Co. Ltd. v Anuj Joshi & Others, *Supreme Court of India. Reply*  
765 *Affidavit on Behalf of Respondent/State of Uttarakhand to I.A. No. 28979 of 2020* (2020).
- 766 99. D. Mishra, Power Ministry Wanted to Dilute Rules So Hydro Projects Can Release Even  
767 Less Water. *The Wire* (2021), (available at [https://thewire.in/government/power-](https://thewire.in/government/power-ministry-dilute-environmental-flow-rules-so-hydro-projects)  
768 [ministry-dilute-environmental-flow-rules-so-hydro-projects](https://thewire.in/government/power-ministry-dilute-environmental-flow-rules-so-hydro-projects)).
- 769 100. M. J. Froude, D. N. Petley, Global fatal landslide occurrence from 2004 to 2016. *Natural*  
770 *Hazards and Earth System Sciences*. **18**, 2161–2181 (2018).
- 771 101. A. Stäubli, S. U. Nussbaumer, S. K. Allen, C. Huggel, M. Arguello, F. Costa, C.  
772 Hergarten, R. Martínez, J. Soto, R. Vargas, E. Zambrano, M. Zimmermann, in *Climate*  
773 *Change, Extreme Events and Disaster Risk Reduction: Towards Sustainable*  
774 *Development Goals*, S. Mal, R. B. Singh, C. Huggel, Eds. (Springer International  
775 Publishing, Cham, 2018; [https://doi.org/10.1007/978-3-319-56469-2\\_2](https://doi.org/10.1007/978-3-319-56469-2_2)), *Sustainable*  
776 *Development Goals Series*, pp. 17–41.
- 777 102. A. Pralong, M. Funk, On the instability of avalanching glaciers. *Journal of Glaciology*.  
778 **52**, 31–48 (2006).
- 779 103. M. Van Wyk de Vries, *MaxVWDV/glacier-image-velocimetry: Glacier Image*  
780 *Velocimetry (GIV)* (2021);  
781 [https://zenodo.org/record/4548848/preview/MaxVWDV/glacier-image-velocimetry-](https://zenodo.org/record/4548848/preview/MaxVWDV/glacier-image-velocimetry-v0.8.0.zip)  
782 [v0.8.0.zip](https://zenodo.org/record/4548848/preview/MaxVWDV/glacier-image-velocimetry-v0.8.0.zip)).

- 783 104. M. Van Wyk de Vries, A. D. Wickert, Glacier Image Velocimetry: an open-source  
784 toolbox for easy and rapid calculation of high-resolution glacier velocity fields. *The*  
785 *Cryosphere*, 1–31 (2021).
- 786 105. S. van der Walt, J. L. Schönberger, J. Nunez-Iglesias, F. Boulogne, J. D. Warner, N.  
787 Yager, E. Gouillart, T. Yu, scikit-image: image processing in Python. *PeerJ*. **2**, e453  
788 (2014).
- 789 106. D. E. Shean, O. Alexandrov, Z. M. Moratto, B. E. Smith, I. R. Joughin, C. Porter, P.  
790 Morin, An automated, open-source pipeline for mass production of digital elevation  
791 models (DEMs) from very-high-resolution commercial stereo satellite imagery. *ISPRS*  
792 *Journal of Photogrammetry and Remote Sensing*. **116**, 101–117 (2016).
- 793 107. R. A. Beyer, O. Alexandrov, S. McMichael, The Ames Stereo Pipeline: NASA’s open  
794 source software for deriving and processing terrain data. *Earth and Space Science*. **5**,  
795 537–548 (2018).
- 796 108. P. Lacroix, Landslides triggered by the Gorkha earthquake in the Langtang valley,  
797 volumes and initiation processes. *Earth, Planets and Space*. **68** (2016),  
798 doi:10.1186/s40623-016-0423-3.
- 799 109. R. Hoste-Colomer, L. Bollinger, H. Lyon-Caen, L. B. Adhikari, C. Baillard, A. Benoit,  
800 M. Bhattarai, R. M. Gupta, E. Jacques, T. Kandel, B. P. Koirala, J. Letort, K. Maharjan,  
801 R. Matrau, R. Pandey, C. Timsina, Lateral variations of the midcrustal seismicity in  
802 western Nepal: Seismotectonic implications. *Earth and Planetary Science Letters*. **504**,  
803 115–125 (2018).
- 804 110. F. Dammeier, J. R. Moore, F. Haslinger, S. Loew, Characterization of alpine rockslides  
805 using statistical analysis of seismic signals. *Journal of Geophysical Research: Earth*  
806 *Surface*. **116**, F04024 (2011).
- 807 111. F. Fuchs, W. Lenhardt, G. Bokelmann, the AlpArray Working Group, Seismic detection  
808 of rockslides at regional scale: examples from the Eastern Alps and feasibility of  
809 kurtosis-based event location. *Earth Surface Dynamics*. **6**, 955–970 (2018).
- 810 112. J. Deparis, D. Jongmans, F. Cotton, L. Baillet, F. Thouvenot, D. Hantz, Analysis of rock-  
811 fall and rock-fall avalanche seismograms in the French Alps. *Bulletin of the*  
812 *Seismological Society of America*. **98**, 1781–1796 (2008).
- 813 113. C. Hibert, A. Mangeney, G. Grandjean, N. M. Shapiro, Slope instabilities in Dolomieu  
814 crater, Réunion Island: From seismic signals to rockfall characteristics. *Journal of*  
815 *Geophysical Research: Earth Surface*. **116**, F04032 (2011).
- 816 114. G. Le Roy, A. Helmstetter, D. Amitrano, F. Guyoton, R. L. Roux-Mallouf, Seismic  
817 analysis of the detachment and impact phases of a rockfall and application for estimating  
818 rockfall volume and free-fall height. *Journal of Geophysical Research: Earth Surface*.  
819 **124**, 2602–2622 (2019).

115. A. Burtin, L. Bollinger, R. Cattin, J. Vergne, J. L. Nábělek, Spatiotemporal sequence of Himalayan debris flow from analysis of high-frequency seismic noise. *Journal of Geophysical Research: Earth Surface*. **114** (2009), doi:<https://doi.org/10.1029/2008JF001198>.
116. G. Monsalve, A. Sheehan, V. Schulte-Pelkum, S. Rajaure, M. R. Pandey, F. Wu, Seismicity and one-dimensional velocity structure of the Himalayan collision zone: Earthquakes in the crust and upper mantle. *Journal of Geophysical Research: Solid Earth*. **111** (2006), doi:<https://doi.org/10.1029/2005JB004062>.
117. Z. Zhang, S. Klemperer, Crustal structure of the Tethyan Himalaya, southern Tibet: new constraints from old wide-angle seismic data. *Geophysical Journal International*. **181**, 1247–1260 (2010).
118. D. Farinotti, M. Huss, J. J. FÜRST, J. Landmann, H. Machguth, F. Maussion, A. Pandit, A consensus estimate for the ice thickness distribution of all glaciers on Earth. *Nature Geoscience*. **12**, 168–173 (2019).
119. T. H. Assumpção, I. Popescu, A. Jonoski, D. P. Solomatine, Citizen observations contributing to flood modelling: opportunities and challenges. *Hydrology and Earth System Sciences*. **22**, 1473–1489 (2018).
120. M. Mergili, J.-T. Fischer, J. Krenn, S. P. Pudasaini, r.avaflow v1, an advanced open-source computational framework for the propagation and interaction of two-phase mass flows. *Geoscientific Model Development*. **10**, 553–569 (2017).
121. M. Mergili, S. P. Pudasaini, r.avaflow - The mass flow simulation tool (2020; <https://www.avaflow.org/>).
122. S. P. Pudasaini, M. Mergili, A multi-phase mass flow model. *Journal of Geophysical Research: Earth Surface*. **124**, 2920–2942 (2019).
123. S. Gascoin, M. Grizonnet, M. Bouchet, G. Salgues, O. Hagolle, Theia Snow collection: high-resolution operational snow cover maps from Sentinel-2 and Landsat-8 data. *Earth System Science Data*. **11**, 493–514 (2019).
124. Uttarakhand DMMC, “List of Missing Persons” (Uttarakhand Disaster Mitigation and Management Centre (DMMC), Dehradun, 2021).

**Acknowledgements:** We acknowledge all the individuals who shared videos, images, and other ‘on-the-ground’ observations in real-time and soon after the event. These eyewitness accounts greatly aided our interpretations. This study was coordinated with the IACS and IPA Standing Group on Glacier and Permafrost Hazards in Mountains (<http://www.gaphaz.org>). PlanetLabs, Maxar, and CNES provided prioritized satellite tasking and rapid data access and for that, we are grateful. We thank the NGA EnhancedView Program Management Office for supporting Level-1B image access under the NextView License and composite DEM release. Any use of trade, firm, or product names is for descriptive purposes only does not imply



endorsement by the U.S. Government. The views and interpretations in this publication are those of the authors and are not necessarily attributable to their organizations. We thank three anonymous reviewers for their insightful comments, which strengthened this paper. Finally, this paper is dedicated to those who lost their lives in the Chamoli disaster, and those who remain missing.

#### Funding:

- Alexander von Humboldt Foundation, Government of the Federal Republic of Germany (AM)
- Centre National d'Études Spatiales internal funding (EB)
- Centre National d'Études Spatiales, Programme National de Télédétection Spatiale PNTS-2018-4 (SG)
- CIRES Graduate Research Fellowship (MJ)
- Department of Science and Technology, Government of India (AKumar, KS)
- European Space Agency CCI programme and EarthExplorer10 4000123681/18/I-NB, 4000109873/14/I-NB, 4000127593/19/I-NS, 4000127656/19/NL/FF/gp (AKääb)
- European Space Agency Glaciers CCI+ 4000127593/19/I-NB (FP)
- Future Investigators in NASA Earth and Space Science and Technology 80NSSC19K1338 (SB)
- ICIMOD core funds (JS)
- Natural Sciences and Engineering Research Council (NSERC) 04207-2020 (DHS)
- NASA Cryosphere 80NSSC20K1442 (UKH, JSK)
- NASA High Mountain Asia Team (HiMAT-1) 80NSSC19K0653 (UKH, JSK, DHS)
- NASA High Mountain Asia Team (HiMAT-2) 80NSSC20K1594 (SR)
- NASA High Mountain Asia Team (HiMAT-2) 80NSSC20K1595 (DES)
- NASA Interdisciplinary Research in Earth Science 80NSSC18K0432 (UKH, JSK)
- Roshydromet R&D Plan, Theme 6.3.2 AAAA-A20-120031990040-7 (MD)
- Swiss Agency for Development and Cooperation (SDC) 7F-08954.01.03 (SA, HF, CH)
- Swiss National Science Foundation 200020\_179130 (JF)
- Swiss National Science Foundation, project "Process-based modelling of global glacier changes (PROGGRES)", Grant Nr. 200021\_184634 (DF)
- Swiss Federal Excellence Postdoc Award (AS)

**Author contributions:** (main author list order preserved for each section): **(1) Writing – original draft:** DHS, MJ, DS, SB, KU, SM, MVWdV, MMergili, AE, EB, JLC, JJC, SAD, HF, SG, UKH, CH, AKääb, JSK, JLK, PL, DP, SR, ME, DF, JN; **(2) Writing – review & editing:** all authors; **(3) Methodology, Investigation, Formal analysis** – satellite-based geomorphological mapping: DHS, WS, JLC, JJC, MD, SAD, UKH, CH, AKääb, SJC, FP, MJW; flow modeling: AS, MM, UKH; energy-balance modeling: AKääb, JSK, JLK; DEM production: DS, SB, CDB, EB, SG; climate, weather, and geology analysis: MJ, DS,

MMcDonnell, RB, SA, HF, UKH, JSK, SG, SR, APD, JF, MK, SL, SM, JN, UM, AM, IR, JS; social and economic impacts: KU, SM, SAD, JSK, MFA, ME; video analysis: AE, FP; precursory motion: MVWdV, SG, AKääb, MD; seismology: PL, MJ; field mapping: MFA, AKumar, IR, KS; **(4) Data curation** – DHS, DS, SB, WS, MVWdV, MMergili, CDB, MMcDonnell, EB, SG, JLK, PL, SR, MJ; **(5) Visualization** – DHS, MJ, DS, SB, WS, MVWdV, MM, AE, CDB, EB, SG, AKääb, JLK, PL, DF; **(6) Project administration** – DHS.

**Competing interests:** Authors declare that they have no competing interests.

**Data availability:** We used publicly available data sources whenever possible. The Sentinel-2 data are available from (57). PlanetScope satellite image data are available through Planet’s Education and Research Program (58). Pre- and post-event very-high resolution satellite images are available through Maxar’s Open Data Program (59), with others available via the NGA NextView License. Airbus/CNES (Pléiades) images were made publicly available through the International Charter: Space and Major Disasters. The derived DEM Composite data are available from (60, 61). ERA5 data are available from the Copernicus climate Data Store.

**Code availability:** The r.avaflow model is available at (62). The r.avaflow code used for the simulation, the start script, and all of the input data are available at [insert link when available] along with a brief tutorial on how to reproduce the results presented in the paper.

## Supplementary Materials

Supplementary Text  
Materials and Methods  
Figs. S1 to S17  
Tables S1 to S5  
References (62-124)



## Supplementary Materials for

A massive rock and ice avalanche caused the 2021 disaster at Chamoli, Indian Himalaya

**Authors:** Shugar, D.H.<sup>1\*</sup>, Jacquemart, M.<sup>2</sup>, Shean, D.<sup>3</sup>, Bhushan, S.<sup>3</sup>, Upadhyay, K.<sup>4</sup>, Sattar, A.<sup>5</sup>, Schwanghart, W.<sup>6</sup>, McBride, S.<sup>7</sup>, Van Wyk de Vries, M.<sup>8,9</sup>, Mergili, M.<sup>10,11</sup>, Emmer, A.<sup>10</sup>, Deschamps-Berger, C.<sup>12</sup>, McDonnell, M.<sup>13</sup>, Bhambri, R.<sup>14</sup>, Allen, S.<sup>5,15</sup>, Berthier, E.<sup>16</sup>, Carrivick, J.L.<sup>17</sup>, Clague, J.J.<sup>18</sup>, Dokukin, M.<sup>19</sup>, Dunning, S.A.<sup>20</sup>, Frey, H.<sup>5</sup>, Gascoin, S.<sup>12</sup>, Haritashya, U.K.<sup>21</sup>, Huggel, C.<sup>5</sup>, Kääb, A.<sup>22</sup>, Kargel, J.S.<sup>23</sup>, Kavanaugh, J.L.<sup>24</sup>, Lacroix, P.<sup>25</sup>, Petley, D.<sup>26</sup>, Rupper, S.<sup>13</sup>, Azam, M.F.<sup>27</sup>, Cook, S.J.<sup>28,29</sup>, Dimri, A.P.<sup>30</sup>, Eriksson, M.<sup>31</sup>, Farinotti, D.<sup>32,33</sup>, Fiddes, J.<sup>34</sup>, Gnyawali, K.R.<sup>35</sup>, Harrison, S.<sup>36</sup>, Jha, M.<sup>37</sup>, Koppes, M.<sup>38</sup>, Kumar, A.<sup>39</sup>, Leinss, S.<sup>40,41</sup>, Majeed, U.<sup>42</sup>, Mal, S.<sup>43</sup>, Muhuri, A.<sup>12,44</sup>, Noetzli, J.<sup>34</sup>, Paul, F.<sup>5</sup>, Rashid, I.<sup>42</sup>, Sain, K.<sup>39</sup>, Steiner, J.<sup>45,46</sup>, Ugalde, F.<sup>47,48</sup>, Watson, C.S.<sup>49</sup>, Westoby, M.J.<sup>50</sup>

Correspondence to: [daniel.shugar@ucalgary.ca](mailto:daniel.shugar@ucalgary.ca)

### This PDF file includes:

Supplementary Text  
Materials and Methods  
Figs. S1 to S17  
Tables S1 to S5

## Supplementary Text

### 1. Study Site

Ronti Peak (6063 m asl) is located in the Nanda Devi Biosphere Reserve, which is amongst UNESCO's world network of Biosphere Reserves, and is in the northern Indian state of Uttarakhand (Fig. 1). The failure zone is within the Reserve's Core Zone, and the impacted people and infrastructure - in Raini and Tapovan villages - are within the Buffer Zone (63).

Geology: The landslide originated in the Joshimath Formation, a basal unit of the Vaikrita Group (64), which is the hanging wall of the Vaikrita Thrust fault (65). The Joshimath Formation consists of high-grade metamorphic rocks, including Precambrian upper amphibolite facies (66), largely psammitic schist and gneiss derived from former impure sandstone. The failure appears to be a bedrock wedge failure, which normally takes place along intersecting rock type or structural discontinuities (67, 68). The failure appears to involve four distinct planar surfaces: the vertical back wall, the detachment surface base, and two lateral intersecting planes. The four surfaces might consist of any combination of bedding planes, foliation, fault planes, and joints (fractures).

High-resolution satellite images of the ice-free south face of Ronti Peak show numerous shear fractures, in addition to stratification or foliation of the metamorphic rocks. The Vaikrita Thrust (69) nominally is 1-2 km west of the failure site. However, the mapped fault is an approximation. With the rugged topography and shallow fault plane dip, the actual surface trace has a complex geometry. This thrust fault must also exist less than 1 km beneath Ronti Peak. Activity on the fault mostly ceased in the Miocene or earlier (65, 70). The primary ongoing seismicity, such as the 1999 Chamoli earthquake, stems from movement associated with the Main Himalayan Thrust, about 16 km beneath the Chamoli area (71). The influence of erosion on this rock sequence is evident in high-resolution satellite images, which show a very rugged relief on the sheared, bedded rocks. This combination of steep slopes, high relief, and faulted and jointed bedded/foliated rocks - including mechanically contrasting rocks juxtaposed on planar contacts - is associated with failures of the greatest magnitude (72). An implied high abundance of platy minerals (e.g., muscovite and biotite) and other fine-grained minerals, and possible chemical weathering, may have made these rocks more prone to disintegration, perhaps contributing to the dynamics of the mass movement.

Climatology: The area is dominated by western disturbances in the winter and the Indian monsoon during summer, with most precipitation falling between June and September. The long term mean based on downscaled ERA-5 shows that near-surface air temperatures at the height of the detachment are sub-freezing for most of the year (fig. S1A). ERA5 data further show a temperature increase of 0.18 °C per decade since 1979 (fig. S1B). A long-term increase in air temperature can also be seen in data from a weather station ~100 km south of Ronti Peak (fig. S1C). The late monsoon and post-monsoon season 2020 stand out from the long term ERA5 record as particularly warm months before returning to more average conditions early winter. Above-freezing temperatures at the elevation of the failure may have provided additional meltwater and contributed to increased freeze-thaw action during the months before the failure (fig. S1A).

**Fig. S1. Historical climate trends.** (A) Long-term mean annual cycle of near surface air temperature at the location of the failure as compared to the year 2020 from downscaled ERA5 data using the TopoSCALE scheme (73). (B) Local mean annual air temperature (MAAT) at the elevation of the failure and (C) Temperature deviations from the long-term mean at an automated weather station at Mukteswar, Kumaon, about 100 km south of Ronti Peak. Data from NOAA Global Historical Climatology Network. ([https://data.giss.nasa.gov/cgi-bin/gistemp/stddata\\_show\\_v4.cgi?id=IN023420800&dt=1&ds=14](https://data.giss.nasa.gov/cgi-bin/gistemp/stddata_show_v4.cgi?id=IN023420800&dt=1&ds=14))

The numerous glaciers in the region are experiencing mass loss, with both thinning and retreat (74, 75), in large part due to the long-term warming trend (76). Geodetic mass balance data derived from recent and historical stereo-imagery (44, 45, 77) were updated and compiled in the present study for Uttarakhand state. The results show that the glacier mass balance rate across Uttarakhand was  $-0.26 \pm 0.12$  m w.e.  $\text{yr}^{-1}$  for the period 1975-2000 and has been ~25% more negative during the period 2000-2018. Regionally, the lower boundary of permafrost is likely between 4000 and 4500 m asl (47, 78). For steep topography, however, the permafrost distribution is crucially influenced by solar radiation. Gruber et al. (4) state that south faces in central and eastern Hindu Kush Himalaya can be permafrost-free up to well above 6000 m asl. The north face of Ronti Peak supports several small hanging glaciers, and the one just west of the failure zone produced large ice avalanches (several million  $\text{m}^3$ ) in the years 2000 and 2016 (fig. S2).

## 2. Social and Economic Impacts

At least 204 people are confirmed dead or remain missing. Complicated rescue efforts involved the use of heavy machinery to search for an estimated 35 people in a large tunnel under construction for the Tapovan project (33). The primary economic cost of the disaster includes over 206 million USD from damage to the 520 MW Tapovan project (34). Losses at the smaller 13.2 MW Rishiganga project are estimated to be at least 17.2 million USD (35). NTPC Limited (79) has pledged financial compensation to the families of workers who were killed, and government agencies pledged compensation for all the killed or injured. Linear infrastructure damage includes six bridges (33) (e.g. fig S15D). The full economic losses are yet to be publicly reported.

### 2.1 Warning systems

After the recent event, a flood warning system was installed 400 m upstream of Raini village (80), primarily to warn of any outburst from a newly formed landslide-dammed lake in the Rishiganga valley (fig. S15D). Unlike glacial lake outburst floods, there is far less certainty in assessing the risk from a hazard cascade like the February 7 event, especially in the event of failure of a secondary landslide-dammed lake (81, 82). The rapidity of this event means that even if such a system had been in place upstream, the warning time would only have been 6-10 minutes, or perhaps up to 20 minutes if the system were installed near the mountain peaks, where a continuing hazard may exist. This would have potentially been enough time that some of those who were killed or injured could have moved to safe ground. While such systems are relatively easy to install, disseminating reliable warnings to people who would respond appropriately is a complex endeavor (54). Pollock and Wartman (56) argue that human behavior is the most significant factor in landslide mortality. Early warning systems, drills,

and public education campaigns for workers and residents are critical for success (55). Furthermore, in the case of tunnel-based infrastructure, such as that at the Tapovan project, effective warnings would have to be transmitted to workers inside the tunnels, and a means of rapid escape incorporated in the tunnel designs to markedly reduce a repeat of this disaster's human toll.

## **2.2 Conservation-development dilemma**

The disaster has returned focus on the Raini village and its famous Chipko Movement, with the media reminiscing the village's struggle for conservation and assertion of residents' rights to their forests (83). Raini, in Uttarakhand's Chamoli district, was the first settlement to be greatly impacted by the mass flow. The village includes two settlements on opposite sides of the Rishiganga River—Raini Chak Subhai, and Raini Chak Lata. Between them is the Rishiganga hydropower project, where 53 people were either killed or remain missing because of the disaster. The village is important in the history of environmental social movements, because in March 1974, women from Raini, led by Gaura Devi, drove away tree fellers engaged in commercial forestry (84). The Chipko Movement is named after residents hugging trees to save them from being cut ('chipko' in Hindi means to cling or hug). The movement, which started in 1973, and witnessed an important manifestation in Raini in 1974, spread across the Garhwal and Kumaon Himalaya. The awareness it created was key to the creation of India's Forest (Conservation) Act, 1980 (85). However, Raini's battle for conservation continues, as its citizens were in the Uttarakhand High Court as recently as April 2019, for an alleged violation of their rights by the Rishiganga project developers, regarding dumping of waste in the river, the use of explosives, and illegal mining (20).

At least 16 major disasters from floods due to heavy rain or glacial lake outburst floods, landslides, and earthquakes have occurred in the Garhwal and Kumaon Himalaya in Uttarakhand between 1894 and 2021 (14, 15). Environmental conservation is an essential component when studying such disasters. A 1970 flood in the Alaknanda catchment, of which Raini is a part, killed 55 people (85). Studies concluded that deforestation was one of the reasons for the massive sediment load brought down in the flood (84, 86). Raini's struggle against floods continues; the Rishiganga project, which was damaged by flooding in 2013 and 2016, is now completely destroyed (35).

The Chamoli disaster has returned attention to large infrastructure projects, including dams (87, 88) and tunnels. Past studies provide some perspective on hydropower development in Uttarakhand. An Expert Body was formed at the behest of the Supreme Court of India after a rainfall-induced disaster in June 2013 killed over 4000 people, and damaged much infrastructure, including hydropower projects (12, 89). The Expert Body's report (89) documented how hydropower projects had exacerbated the 2013 disaster. Sediment dumping and the use of explosives by dam construction companies were specifically mentioned as causing harm to the fragile Himalayan environment. The report mentions at least three environmental concerns with respect to the Tapovan Vishnugad project, which was damaged in the recent disaster. First, the project, which is located in the Buffer Zone of the Nanda Devi Biosphere Reserve, poses a potential threat to the region's biodiversity and habitats. Second, sediment disposal was mismanaged at the dam site. Third, on December 24, 2009, tunneling intersected an aquifer and discharged at least 60 million litres of water, daily, for over one month (90). The project was also damaged in the 2012, 2013 and 2016 floods (91, 92).

1103 Additionally, there has been public discontent regarding the lack of community participation  
1104 in the decision-making process for the project (19). The importance of seeking public opinion  
1105 in hydropower projects in the Himalaya has been stressed by Grönwall (93).

1106 Seismicity is an important consideration when locating and constructing hydropower projects  
1107 in the Himalaya as many Himalayan regions, including Uttarakhand, India, are vulnerable to  
1108 large earthquakes (94, 95). The Mw 7.8 Gorkha earthquake in Nepal in 2015 damaged 16  
1109 hydropower projects with a total installed capacity of 270 MW (95). Several hydropower  
1110 projects in the Himalaya are in the planning stage and need to take seismicity into  
1111 consideration, including the proposed 5040 MW Pancheshwar project on the Mahakali River  
1112 between Uttarakhand, India and westernmost Nepal (96). Especially important, in our view, is  
1113 to consider seismically triggered hazards cascades and the potential for long-runout events  
1114 such as experienced in Chamoli.

1115 Data from 2013 show that the Uttarakhand government was planning 450 hydropower  
1116 projects with a combined generating capacity of 27039 MW (89). Of those, 92 projects (3624  
1117 MW) had been commissioned at that time, 38 (3292 MW) were under construction, and 320  
1118 (20123 MW) were either awaiting approval or undergoing surveys (89). However, an ongoing  
1119 case in the Supreme Court of India has slowed dam construction in the state. In a series of  
1120 court cases and filings, the Uttarakhand government has argued about revenue loss (~618  
1121 million USD) from delays in hydropower development and reductions in generating capacity  
1122 of operational hydropower projects due to existing norms (97–99). However, a counter-  
1123 argument may have been made by the tragic disaster in 2021.

1124 In sum, it is apparent that tension between conservation and resistance to development on one  
1125 hand, and pressures to develop on the other hand are very alive in Uttarakhand and other  
1126 Himalayan states. Wide-ranging Earth-system hazards have been displayed intensively in  
1127 repeated disasters in the Himalaya (100, 101). At the same time, India is seeking, as is the rest  
1128 of the world, to reduce dependence on fossil fuels, and hydropower is an obvious choice for  
1129 doing this. The tension thus will not disappear; the question is how to balance the needs.

### 1130 **3. Antecedent conditions**

#### 1131 ***3.1 Past events***

1132 The north face of Ronti Peak has been the site of mass failures in recent decades, although  
1133 most involved only hanging glacier ice (cf. 102). The first event that we catalogued using  
1134 Landsat 7 data occurred between January 3 and April 8, 2000, when part of the hanging  
1135 glacier (~0.16 km<sup>2</sup>) collapsed from an elevation of ~5300 m and descended to the Ronti Gad  
1136 valley (fig. S2). The ice mass traveled a distance of about 6 km and impacted an area of ~0.7  
1137 km<sup>2</sup> on the valley floor. By 2003, the icy avalanche deposits in the valley had mostly melted.

1138  
1139 The second event occurred between September 19 and October 3, 2016 based on Sentinel-2  
1140 and Planet Labs imagery, and involved the same hanging glacier, which had reformed since  
1141 2000 (fig. S2, S3, S5). The glacier again collapsed (~0.2 km<sup>2</sup> source area) from about the  
1142 same elevation, impacted the valley to a distance of ~6.5 km from the source, and had an  
1143 almost identical area to that of the 2000 event. These avalanche deposits had almost entirely  
1144 melted by 2019.

### 3.2 Precursory motion

We calculated precursory slope motion using optical feature tracking model GIV (103, 104). Displacements were calculated across 11012 pairs of Sentinel-2 images, spanning the period from November 2015 to February 2021, and processed into monthly mean velocity maps. We observed over 10 m of slip in the vicinity of the 2021 landslide in the five years that preceded the catastrophic slope failure. There were particularly rapid episodes of slip in the summers of 2017 and 2018 (fig. S4), with displacements of  $>5 \text{ m a}^{-1}$  even in areas of bare bedrock (see also fig. S5).

**Fig. S5. High-resolution orthoimages over source area.** Image sequence includes Maxar/DigitalGlobe WorldView-1/2 (PAN, 0.5 m), ISRO/NRSC CartoSat-1 (PAN, 2.5 m), Planet Dove Classic (NIR, ~3-4 m) and CNES/Airbus Pleiades-HR (PAN, 0.5 m) imagery. See Table S2 for more details. All images except September 10, 2015 were enhanced using a Contrast Limited Adaptive Histogram Equalisation (CLAHE) algorithm implemented in the scikit-image package v0.17.1 (105; clip limit 0.05, kernel size of 500 px for  $<1 \text{ m}$  GSD imagery, 125 px for others) to bring out detail over both light (e.g., ice/snow) and dark (e.g., exposed rock) surfaces. The large fracture associated with the February 7, 2021 event is apparent in the October 19, 2017 image, with increased width in the November 1, 2018 image. Limited expansion is observed in subsequent images. The 2021 images show stratigraphy exposed in the west wall of the scar, and deposits from small rockfall events following the large February 7, 2021 collapse. These orthoimages were derived from Level-1B imagery that is © Maxar/Digitalglobe, Inc. (NGA NextView License), ISRO/NRSC, Planet Labs, Inc., and CNES/Airbus DS. Pre-event images were orthorectified using the September 2015 DEM Composite (60), post-event images were orthorectified using the February 2021 DEM Composite (61).

## Materials and Methods

### 4. Materials

We used multiple stereo observations from very high resolution (DigitalGlobe/Maxar GeoEye-1 and WorldView-1/2/3, CNES/Airbus Pleiades-HR, and Planet SkySat-C, all 0.3-0.7 m GSD) and high-resolution (Airbus SPOT-7, 1.5 m GSD; Cartosat-1, 2.5 m GSD) satellite imagery to produce a time-series of DEMs between 2015 and 2021 (table S2). While several of the satellite images listed in Table S2 were acquired as in-track stereo pairs by the same sensor, we also formed several additional cross-track stereo pairs from monoscopic images acquired within a few days by different sensors on different orbits. All DEMs were generated using the open-source NASA Ames Stereo Pipeline (106, 107), with processing details for the September 2015 pre-event and February 2021 post-event DEM composites described in Bhushan and Shean (60) and Shean et al. (61), respectively. We used similar processing parameters to derive a DEM from the December 24, 2018 SPOT-7 stereo pair (108).



## 5. Methods

### 5.1 Seismological analysis

We analyzed continuous seismic data from two stations (Bayana - noted BAYN - and Ghanteshwar - noted GHAN) of the Nepalese seismic network (DMG/NEMRC) for the days February 6, 2021 and February 07, 2021 (109). BAYN is a short period ( $<2$  s) ZM500 vertical sensor. GHAN is a 3-component broadband velocimeter. Sampling frequencies of these signals are 50 Hz. Goals of the seismic data analysis were to detect any potential events prior to the main flow, characterize the onset time of the rockslide, and constrain the velocity of the flow at its initiation.

We first detected all events recorded simultaneously by the two sensors (locations shown in fig. S6E) by calculating the peaks in the spectrogram stacked in the frequency range 0.5 – 20 Hz, as a function of time. An event is identified when this function exceeds 3. All the peaks separated by less than 20 seconds are considered to be part of the same event. This procedure leads to the detection of two local earthquakes (February 6, 2021 at 17:43, February 7, 2021 at 09:22, UTC), one a Mw3 earthquake located east of Kathmandu (February 7, 2021 04:31, UTC) and characterized by impulsive onsets and clear P- and S-wave arrivals. This detection clearly identified the Chamoli rock and ice avalanche (February 7, 2021 04:52), with clear triangular asymmetrical shapes on the spectrogram of about 5 minutes (fig. S6A-C), typical of large rockslide sources (110, 111). The main frequency content is below 15 Hz and is followed by a long coda of at least 10 minutes (see fig. S6 and table S3), with frequency content below 5 Hz. This unusual long tail suggests the source of this signal is generated by a succession of a rock slope failure followed by a long duration flow.

This detection procedure suggests that no earthquakes dynamically triggered the rock slope failure, and that the block detached in one piece, or at least that the major part of the block detached in this event.

The BAYN signal shows an impulsive onset (fig. S6D), with a clear first signal, different in terms of amplitude and frequency from the seismic noise. Such a first pulse is not seen on the GHAN records due to higher noise of the traces. We therefore interpret this first signal as the detachment phase of the failure, also previously observed with other rockfalls or rockslides (112–114) and created either by elastic rebound of the cliff, fracture opening, or friction between the detached compartment and the cliff. Therefore, this signal gives a clear time constraint of the event onset, with a 2s uncertainty depending on the physical origin of this signal. In the case of the fracture opening hypothesis, a small time delay can exist between this signal and the avalanche initiation. The 2s uncertainty is estimated through the length of the detachment signal.

We corrected this onset time from the wave propagation travel time between source and station by estimating the P-wave apparent velocity through correlation of the two spectrograms at stations BAYN and GHAN. The time-shift between the two signal envelopes is estimated by maximizing the correlation between the two seismic envelopes as a function of

a time-shift (115), leading to a value between 2.56 and 2.05 seconds, depending on whether the raw correlation function or a mathematical fit is used. Given the slight distance difference between the two stations and the event (Table 1), this time-shift provides mean wave apparent velocities between 5.8 and 7.2 km s<sup>-1</sup>. These values are consistent with P-wave velocity estimates of the crust and upper mantle in the high Himalaya (116, 117) and show that P-wave dominates the high-frequency content of the signal. The wave propagation travel-time is consequently estimated at between 24.2 and 30.0 seconds at station BAYN, providing an onset time of the rockslide detachment between 4:51:13 and 04:51:21 UTC, including the error on the physical origin of the detachment signal.

The two spectrograms are very well correlated (fig. S6A), including several high-frequency peaks created by impacts of the flow on valley flanks, turns, and changes of slope gradient. The first major peak occurs 55 to 58 seconds after detachment (fig. S6A, B).

Given the topographic profile of the initial slope, with no large depressions, bumps, or major turns, this signal certainly comes from the impact of the flow on the northeastern flank of the valley. This analysis allows us to calculate the velocity of the avalanche as it descends from the detachment scar to the valley floor, an average speed of 57 to 60 m s<sup>-1</sup> (205 to 216 km h<sup>-1</sup>).

## 5.2 Estimation of volume and rock:ice ratio

The volume and ratio of rock and ice involved in the failure are key to understanding the exceptional downstream mobility of the mass flow. We assess the volume of each contribution using pre- and post-event digital elevation models (61, 61) and estimates of ice thickness from our own inversion based on glacier flow velocity and Farinotti et al. (118).

We account for the following uncertainties:

1. DEM vertical uncertainty
2. Collapse area lateral extent
3. Ice thickness

**1)** Collapse volume calculations are based on the difference between pre- and post- event DEMs. The relevant vertical uncertainty is thus the summed uncertainties in the two maps. To evaluate this, we fit a gaussian peak to the difference map in areas with elevations that are known to have not changed (bedrock on the south face of the Ronti ridge). The histogram of stable ground is shown in fig. S7. This histogram can be fit with a gaussian peak with a mean of (+) 0.33 m and a standard deviation of 0.64 m. We use this to estimate the two-sigma DEM differencing uncertainty as 1.28 m.

**2)** We evaluate the uncertainty in collapse area lateral extent by using two contours in the DEM difference map: the -5 m contour and 0 m contour. In theory, if all else is stable, the 0 m contour would delineate the lateral extent of the collapse scar. Visual estimation, however, suggests that this is an overestimate, likely due to snow and to ice thickness changes between the 2015 pre-event DEM and the landslide date, and DEM uncertainty. We thus consider the 0 m contour as a maximum bound for the collapse area and -5 m contour as the minimum bound

(shown in fig. S8). Comparison to pre-event imagery shows that 75% of the region between the 0 and -5 m contours is covered with ice, the remainder being bedrock. We calculate the volume of material removed in this area by differencing the pre- and post-event DEMs.

**3)** We evaluate uncertainties in ice thickness based on two sources: four glacier thickness maps from Farinotti et al. (118) (methods 1-4), and an additional inversion based on glacier surface velocity. For each, we calculate the total ice volume over the collapse area. The result of this analysis is shown in fig. S9. The volume calculated from the velocity-based inversion is 5.38 Mm<sup>3</sup> of ice (95% confidence intervals 4.82-6.35 Mm<sup>3</sup>), with volumes of 6.69, 5.08, 4.57 and 4.13 Mm<sup>3</sup> calculated using the Farinotti et al. (118) methods 1-4, respectively. We average the four Farinotti et al. (118) ice volume estimates, and assign the composite a 20% (two-sigma) uncertainty. Uncertainties in ice velocity and inversion parameters are already accounted for in the ice velocity-based inversion. These volume estimates do not include the area between the 0 and -5 m contours, which is estimated separately.

We then calculate the total landslide volume ( $V_T$ ), volume of rock ( $V_R$ ), and rock percentage ( $R_R$ ) using the three following equations:

$$V_T = (DEM1_{(<x)} - DEM2_{(<x)} \pm U_T) * A_{(<x)} \quad (1)$$

$$V_R = V_T - V_I \quad (2)$$

$$R_R = \frac{100V_R}{V_R + V_I} \quad (3)$$

where DEM1 and DEM2 are the 2015 and 2021 DEMs within difference contour level x, A is the area of the collapse within contour level x, x is a number selected from a uniform distribution between 0 and -5 (accounting for uncertainty in collapse area lateral extent),  $U_T$  is a DEM difference uncertainty term (randomly selected from a normal distribution with two standard deviations equal to 1.28 m), and  $V_I$  is the ice volume selected randomly from the either the Farinotti et al. (118) composite or ice velocity-based inversion (in both cases, accounting for uncertainties). Uncertainties are handled using a Bayesian approach, with 100,000 runs.

The results are shown in fig. S10. In summary, we have:

- A total landslide volume of 26.9 Mm<sup>3</sup> [95% confidence intervals (CI) 26.5-27.3 Mm<sup>3</sup>]
- A volume of rock of 21.4 Mm<sup>3</sup> [95% CI 20.4-22.2 Mm<sup>3</sup>]
- An ice volume of 5.5 Mm<sup>3</sup> [95% CI 4.7-6.4 Mm<sup>3</sup>]
- A rock percentage in the collapse of 79% [95% CI 76-82%]

### 5.3 Insights into flow characteristics and timing from eyewitness videos

We explored available eyewitness videos published on Facebook and YouTube and searched for videos capturing the arrival of the flow front at different locations along the flow path (table S4), to reconstruct timing, dynamics, and magnitude of the disaster cascade (e.g. 119).

Analysis of flow-front velocity and discharge involved three steps: (1) the location of the camera and viewed scene were determined based on identifiable buildings, bridges, roads, and geomorphic features (ridges, rills, boulders) with cross-validation provided by high-resolution satellite images and field photos; (2) mean flow velocity ( $v$ ) was estimated as a quotient of flow travel distance ( $\Delta d$ ) and time ( $\Delta t$ ) ( $v = \Delta d / \Delta t$ );  $\Delta d$  was determined from high-resolution satellite images (streamline distance), and  $\Delta t$  was derived from the videos (table S4); (3) mean discharge of the flow front was calculated as a product of the mean flow velocity ( $v$ ) and cross-profile area of the flow ( $A$ );  $A$  was approximated by the area of an idealized trapezoid with the underside of the trapezoid taken to be the mean active channel width along the analyzed section of the stream, and  $45^\circ$  and  $60^\circ$  the stream bank steepness. The depth for calculating cross-sectional area was approximated from eyewitness videos where appropriate (e.g. where buildings located on the banks gave sense of scale). Where this was not appropriate, we measured pre- and post-event channel width (bottom and top side of idealized trapezoid) and approximated depth by assuming side inclination of  $45^\circ$  to  $60^\circ$ . This resulted in mean flow depths ranging from 7 to 13 m. We did not use mapped trimlines to estimate flow depths for approximating  $A$  because of potential major overestimation caused by unsteady flow character and upslope runup. The outcomes of steps (1) and (2) are generally reliable; step (3) has the largest uncertainty, mainly resulting from the estimation of  $A$ .

The timing of the flow front arrival at specific locations (absolute timing  $T$ ) was determined using: (1) times of videos streamed live on Facebook; and (2) metadata of selected videos provided by the authors. Further, we approximated times of the flow front arrival at a variety of locations along the streamline from  $T$  and estimated flow front velocities  $v$ .

We estimated flow front velocity at four sites, P1 to P4, located 14.3 to 25.7 km downstream from the source (fig. S11, table S5). The absolute time of the flow front arrival is only known for the Tapovan site, where the flow front appeared at 10:38 – 10:39.

#### **5.4 Simulation of the flow evolution with *r.avaflow***

Computer simulations were performed to test the plausibility of initial hypotheses of flow evolution, with the aim of rejecting some hypotheses and therefore better constraining viable mechanisms. The open-source GIS-based mass flow simulation tool *r.avaflow* was used for the simulations (120, 121). The multi-phase model of Pudasaini and Mergili (122) was used to simulate the process chain from the release of the initial rock/ice avalanche to location P4, with two solid phases (rock, ice including some till) and one fluid phase (water and fine mud). The ice phase was transformed to fluid at a rate proportional to the flow kinetic energy. Initial conditions were given by the DEM, the release mass ( $21.4 \times 10^6 \text{ m}^3$  of rock and  $5.5 \times 10^6 \text{ m}^3$  of ice), and different amounts of entrainable material (debris, snow assumed to melt immediately, and/or soil water), depending on the scenario. The flow parameters were optimized based on empirical data (trimlines to check flow extent, reconstructed peak discharges, frontal velocities, and travel times). Four zones with specific parameter sets were defined along the flow path: initial rock/ice avalanche, Ronti Gad, Rishiganga, and Dhauliganga (fig. S12). We note that the simulation mainly aimed to reproduce the frontal

part of the flow until peak discharge. No detailed reference information, and therefore no bases for evaluating the simulation, is available for the flow tail.

The transformation from a rock and ice avalanche into a debris flow was a complex process, the simulation of which had to rely on some simplifications and assumptions. In the simulation shown in Fig. 4, at  $t=480$  s, the front of the debris flow had escaped far down Rishiganga. The simulated rock and ice avalanche had reached the observed deposit at and downstream from the Ronti Gad-Rishiganga confluence, and had largely come to rest according to visual inspection of the results. In order to avoid further diffusion (which would be the result of the numerical scheme used in the model rather than of the physical processes), the avalanche is deposited at this point in time, but fluid and ice continue to flow out of the frontal portion of the deposit together with an amount of rock equalling the amount of fluid, in this way representing a uniform debris flow tail.

Preliminary tests have shown that most observed features could be reproduced at a simulation cell size of 20 m down to the lower Rishiganga valley, whereas a cell size of 10 m was necessary to reproduce the flow characteristics from the Rishiganga – Dhauliganga confluence downstream. In order to optimize computational efficiency, the simulation was split into two parts: the first part (20 m cell size) focusing on the domain down to the lower part of Rishiganga, and the second part (10 m cell size) on the area downstream. The output hydrograph from the first part of the simulation at P1 is directly used as the input hydrograph for the second simulation.

The simulated process time included the first 1300 s following the release of the initial rock and ice avalanche for the first part, and 2100 s from the onset of discharge at P1 for the second part. Peak discharges represent the maximum simulated within 20s time steps (P1 and P2 from the first part, P3 and P4 from the second part of the simulation). Travel times refer to times at which 10% of the peak discharge at a given hydrograph profile has been reached. The evolution of volume fractions and velocities shown in Fig. 4C are smoothed based on moving averages.

### **5.5 Sources of water and energy balance modeling**

We estimate that the initial detachment had a total volume of  $26.7 \text{ Mm}^3$ , composed of  $21.2 \text{ Mm}^3$  rock and  $5.5 \text{ Mm}^3$  ice, and thus a volumetric ratio of 79.4:20.6 (rounded to 80:20 elsewhere). We considered, but then rejected, possible additional sources of liquid water that would have contributed significantly to the volume of the debris flow: (1) An outburst flood from a subglacial lake at either Nanda Devi Glacier or Ronti (aka Raunthi) Glacier, as had been suggested for several days following the event. (Satellite imagery shows no change at the terminus of either glacier that would indicate a subglacial flood; furthermore, there is no plausible mechanism whereby a glacier lake outburst flood could have occurred at the same time as the detachment.) (2) A surface lake in the Rishiganga or Ronti Gad valleys. (Satellite images available up to about 24 h before the event showed no such lake.) (3) A lake in the valley beneath avalanched ice masses. (Ice from 2016 and earlier avalanches had melted completely by 2019, leaving no lakes.) (4) An ice-covered lake within or beneath the collapsed glacier. (The steepness of the detached ice precludes the presence of a lake.) (5) A

possible enlithic lake in the crack that developed in the years preceding failure. (Any meltwater entering this crack would have quickly frozen.) (6) Enlithic reservoirs in bedrock caverns that may have emptied when the avalanche occurred. (In any case, enlithic reservoirs could not account for the millions of m<sup>3</sup> of water involved in the mass flow.) (7) A precursor ice avalanche that deposited ice in the valley in the hours preceding the main detachment. (Only a small volume of water would be produced in a few hours of melting and the seismic signals indicate no major precursory avalanche.)

One additional potential source of water within the initial rock and ice avalanche is precipitation from a slow-moving storm system that brought widespread snowfall to the region in the days before the event and then was followed by an abrupt increase in temperature on the day of the failure. A weather warning was issued for Uttarakhand by the India Meteorological Department on February 1, 2021, predicting rain, snow, and isolated thunderstorms for February 4 and 5. The snow cover map generated from a Sentinel-2 image acquired on February 5 shows snow down to 2200 m on February 5 (e.g. 123). Total precipitation estimates for the period February 4-6 differ widely, with local stations showing cumulative amounts of 8.5 and 14.5 mm at 1800 and 2800 m asl, respectively, and Weather Research and Forecasting Model outputs suggesting amounts of ~48 mm. On the day of the failure, both ERA5 and local weather stations show a temperature increase of about 12°C, with station data suggesting that warming may have been more pronounced at higher elevations due to a temperature inversion affecting the valleys. However, temperatures at the failure zone are estimated to have remained below freezing on the day of the failure (highs between -0.5 to -9°C depending on data source). On February 10, Sentinel-2 data indicate that the snow cover area was reduced by ~50% on south-facing slopes and by ~30% on north-facing slopes.

We estimate the potential total volume of water in the Ronti Gad valley contributed by this storm system by summing the modeled liquid precipitation and melt of snow using data from the Weather Research and Forecasting Model and two local automated weather stations. We make the simplifying assumptions that all precipitation falling at temperatures above 0 °C is instantaneously routed to runoff and that snow melt occurring after deposition (calculated from the solid precipitation amount using a degree-day factor at hourly time resolution and temperature lapse rates ranging from -4 °C km<sup>-1</sup> and -6 °C km<sup>-1</sup>) is similarly routed. The assumption of instantaneous routing provides a likely upper limit to the amount of water the storm system might have contributed to the event.

Total cumulative precipitation and snowmelt amounts derived from these calculations suggest that the available water volume did not exceed ~220,000 – 360,000 m<sup>3</sup> (fig. S13), depending on the lapse rate. We note that although the median lapse rate calculated over the seven days prior to the event using data from the nearest two stations is -5 °C km<sup>-1</sup>, a temperature inversion observed in the region on the day of the event increases the uncertainty of temperature extrapolations. However, given that the calculated total volume of runoff is just 4-7% of the ~5x10<sup>6</sup> m<sup>3</sup> water equivalent contained within the ice of the initial detachment, it is unlikely that precipitation from the storm system was a major source of the large volume of water necessary to sustain flow of the rock/ice/water mixture, regardless of any role weather might have played in the event's initiation.

Water already present in the river, ejected from groundwater, melting snow, wet sediment, and water released from the run-of-the-river hydroelectric project may have all contributed water to the debris flow. Taken together, even with generous margins of error, these sum to a small amount compared to the probable range of water volumes in the mass movement. We do not see mechanisms whereby liquid water was a key component of the initial detachment or where large quantities of water already in the valley could have been ingested.

The melting of glacier ice during the collapse and flow is thus the only known and likely major source of water. Under certain likely conditions it could explain the volume of the observed debris flow, even with only minor contributions from other water sources. This mechanism is a matter of energy accounting (fig. S14), including evaluation of the partitioning of heat transfer.

The gravitational potential energy of the detached rock and ice, plus any mass picked up along the descent route, provides all of the energy for: the movement, acoustic emissions (infrasound, auditory, and seismic), rock and grain fracturing, heating, and melting of ice and heat retention in the rock. The heating and melting energy is commonly referred to as “frictional,” but it is more than slabs sliding against each other; it includes grain sliding and also dissipation of other energies, such as that due to particle impacts, straining and breaking of rock and ice, viscous dissipation in fluids (whether water or air), and emission and reabsorption of acoustic energy. The kinetic movement is not in itself a final sink of energy; rather, kinetic energy is the intermediary by which grain fracturing and heating are achieved by the dissipative processes.

We examine the potential energy released during the event, and whether this energy is sufficient to explain the observed water volumes, using a simple calculation. The gravitational potential energy of an object with mass  $m$  that is lowered by a distance  $\Delta h$  will liberate potential energy in the amount  $P = -mg\Delta h$ , where  $g = 9.8 \text{ m s}^{-1}$  is the acceleration due to gravity. As noted above, it is the potential energy that powers all of the processes associated with the mass movement. Here we assume that only a fraction  $\varepsilon$  of the available potential energy acts to first warm the ice (and a portion of the initial rock volume, as explained below) to the melting point and, subsequently, to melt the ice; for clarity, we call this the “melt partition” of the potential energy, even though it is first applied to warming the ice and a portion of the rock to the ice melting point. The remaining portion  $1 - \varepsilon$  represents the portion of the potential energy that goes towards all other flow-related processes. Assuming that the detached mass has volume  $V$ , a rock fraction of  $f_R = 0.8$ , and ice fraction of  $1 - f_R = 0.2$ , rock and ice densities of  $\rho_R = 2600 \text{ kg m}^{-3}$  (appropriate for gneiss) and  $\rho_I = 900 \text{ kg m}^{-3}$ , respectively, the melt partition of potential energy is

$$P_M = -\varepsilon V \{ f_R \rho_R + [1 - f_R] \rho_I \} g \Delta h \quad (4)$$

We assume that only a fraction  $\gamma$  of the original detachment’s rock volume is required to warm up from an assumed initial temperature of about  $-8^\circ\text{C}$  (the average of the 1980-2020 mean annual air temperatures, Fig. S1B) to  $0^\circ\text{C}$  before melting commences; we assume that

Field Code Changed

Field Code Changed

Field Code Changed

Field Code Changed

Field Code Changed

all of the ice must also warm by the same  $\Delta T = +8^\circ\text{C}$  before melting commences. The amount of energy  $Q_W$  required to warm a mass  $m$  by an amount  $\Delta T$  is proportional to the specific heat capacity  $C$  of the material; mean values for the specific heat capacities of gneiss and ice over the temperature range  $-8^\circ\text{C}$  to  $0^\circ\text{C}$  are, respectively,  $C_R = 850 \text{ J kg}^{-1} \text{ K}^{-1}$  and  $C_I = 2039 \text{ J kg}^{-1} \text{ K}^{-1}$ . The energy needed to warm up the respective volumes of rock and ice are

$$Q_{W,R} = \gamma V f_R \rho_R C_R \Delta T \quad (5)$$

$$Q_{W,I} = V [1 - f_R] \rho_I C_I \Delta T \quad (6)$$

Once the initial detached rock and ice is warmed to  $0^\circ\text{C}$ , all additional potential energy added to the melt partition goes towards melting ice. The energy required to melt the ice volume is

$$Q_M = V [1 - f_R] \rho_I L_I \quad (7)$$

where  $L_I = 3.3355 \times 10^5 \text{ J kg}^{-1}$  is the enthalpy of fusion for ice. It is worth noting that because the specific heat capacities of rock and ice are much smaller than the enthalpy of fusion for ice, the amount of energy needed to warm rock and ice to the melting point is only a small fraction of that needed to melt the ice.

From equations 4-7, we can calculate the fraction of ice melted as  $[P_M - Q_{W,R} - Q_{W,I}] / Q_M$ . For an elevation change of  $\Delta h = -3400 \text{ m}$  (the mean fall distance between the site of initial detachment and the Rishiganga hydropower project),  $\varepsilon = 0.85$ , and  $\gamma = 0.10$ , >99% of the initial ice mass would be melted by the release of potential energy. These calculations suggest even accounting for processes powered by the release of potential energy that do not result in ice melt, sufficient potential energy was liberated in the event to melt most of the  $\sim 5 \text{ Mm}^3$  of ice before it reached the site of the Rishiganga hydropower installation.

It is worth stressing that the two key factors that allowed the major portion of the ice to melt were (1) the particular 80:20 rock:ice ratio of the detachment and (2) the large elevation drop. Because rock is significantly denser than ice, falling rock liberates more potential energy than does an equal volume of falling ice. Neglecting the energy consumed by warming the rock and ice to  $0^\circ\text{C}$  ( $\sim 7\%$  of the energy used in melting ice in the above calculations), we can determine the rock fraction  $\hat{f}_R$  that melts the greatest ice content depending on a mean fall

height  $\Delta \bar{h}$  by combining equations 4 and 7:

$$\hat{f}_R = \frac{L_I - \varepsilon g \Delta \bar{h}}{[\rho_R / \rho_I - 1] \varepsilon g \Delta \bar{h}} \quad (8)$$

Figure S14 shows how this worst-case rock fraction differs as a function of elevation drop for melt partition values of  $\varepsilon = 1.00$  and  $\varepsilon = 0.85$ . It can be seen from this figure that the  $\sim 80:20$  mixture of rock and ice that is thought to have made up the initial detachment is very close to the worst-case scenario for an elevation change of  $\Delta \bar{h} = -3400 \text{ m}$ . Worst-case rock fraction values calculated for this elevation change are  $\hat{f}_R = 0.75$  for  $\varepsilon = 1.00$  and  $\hat{f}_R = 0.79$  for

Field Code Changed

Field Code Changed

Field Code Changed

Field Code Changed

Field Code Changed

Field Code Changed

Field Code Changed

Field Code Changed



$\varepsilon = 0.85$ , values that are close to our estimate for this event. We note that a 80:20 mixture is also typical of debris flows, and thus represents a highly mobile flow.

The availability and generation of water through frictional melting of ice and snow, existing subaerial and subsurface water bodies or saturated sediment, play a critical role in the potential of an event to extend the risk to downstream populations and assets. However, even post-disaster analysis can be challenged by uncertainties in identifying the sources and the role of water. In this case, the major source of the water seems clear. Observations suggest that the initial detachment contained  $5.5 \text{ Mm}^3$  of ice, mixed with an additional  $21.2 \text{ Mm}^3$  of rock. The simple potential energy model described in equations 4-8 suggests that the potential energy released during the descent of the detached rock/ice mass was sufficient to largely melt the volume of ice within the first 10-15 km of its flow, provided that the major part of the released potential energy was consumed by melting the ice and that the melt proceeded rapidly due to the violence of the event. Although additional sources of water might have contributed to the debris flow, they are not necessary to explain the observed event. Our analysis suggests that the mixture of rock and ice in the initial detachment, when combined with the vertical distance it fell, place this event close to a worst-case scenario, maximizing the conversion of potential energy to ice melt and thus the mobility of the resulting flow.

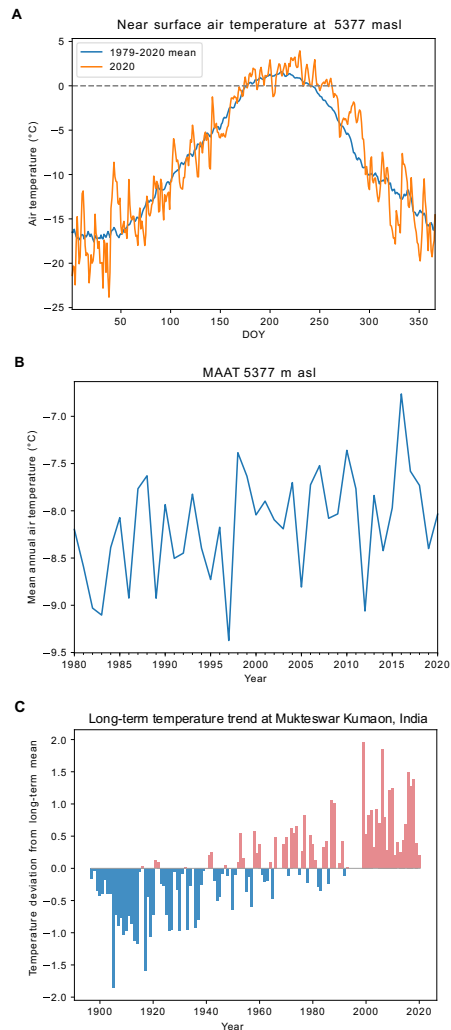


**Fig. S1. Historical climate trends.** (A) Long-term mean annual cycle of near surface air temperature at the location of the failure as compared to the year 2020 from downscaled ERA5 data using the TopoSCALE scheme (73). (B) Local mean annual air temperature (MAAT) at the elevation of the failure and (C) Temperature deviations from the long-term mean at an automated weather station at Mukteswar, Kumaon, about 100 km south of Ronti Peak. Data from NOAA Global Historical Climatology Network. ([https://data.giss.nasa.gov/cgi-bin/gistemp/stddata\\_show\\_v4.cgi?id=IN023420800&dt=1&ds=14](https://data.giss.nasa.gov/cgi-bin/gistemp/stddata_show_v4.cgi?id=IN023420800&dt=1&ds=14))

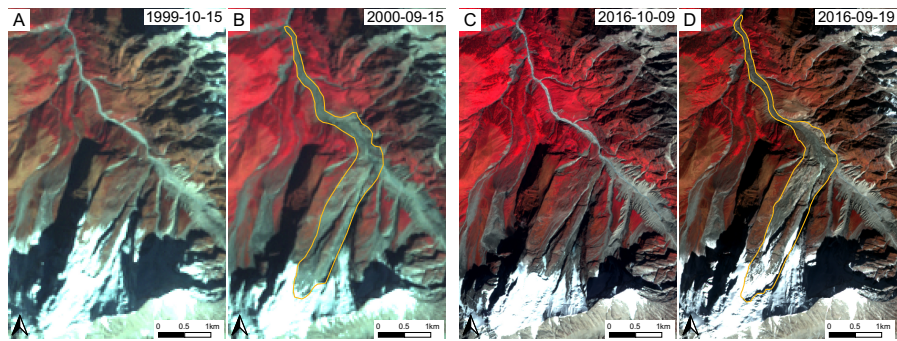


**Fig. S2. Landsat 7 (1999-2000) and Sentinel-2 (2016) images showing the ice avalanches sourced on the hanging glacier west of the failure zone.**

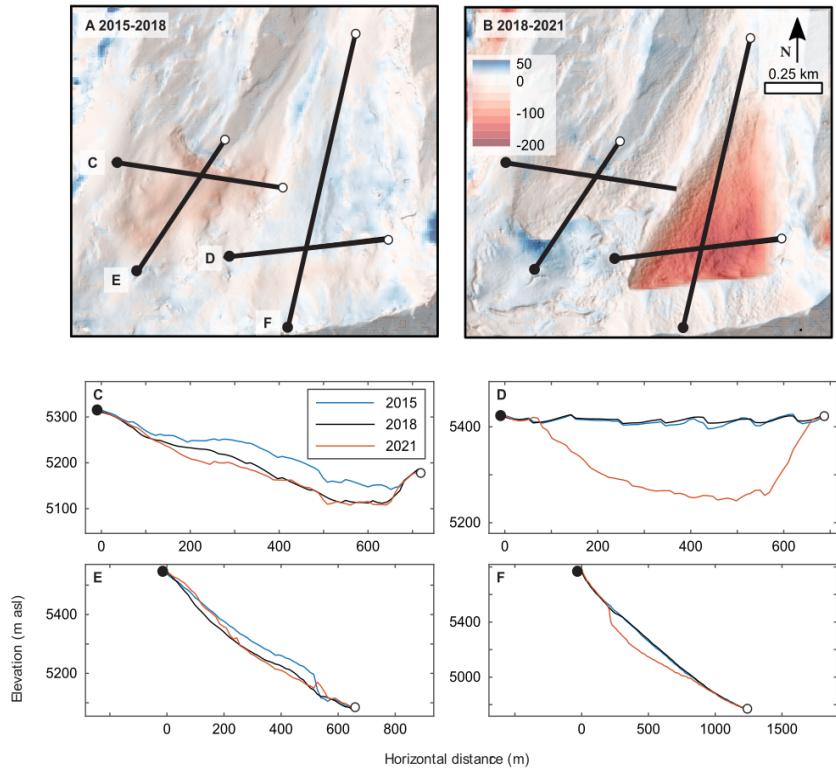


**Fig. S3. Satellite-derived elevation change of the source area.** (A) Elevation change in the source area of the 2016 avalanche based on differences in DEMs between September 2015 and December 24, 2018. Background image is a hillshade view of the September 2015 DEM. (B) Elevation change in the source area of the 2021 ice-rock avalanche based on differences between the December 24, 2018, and February 10-11, 2021 DEM. Background image is a hillshade view of the February 2021 DEM. (C-D) Topographic profiles of locations shown in panels A-B.

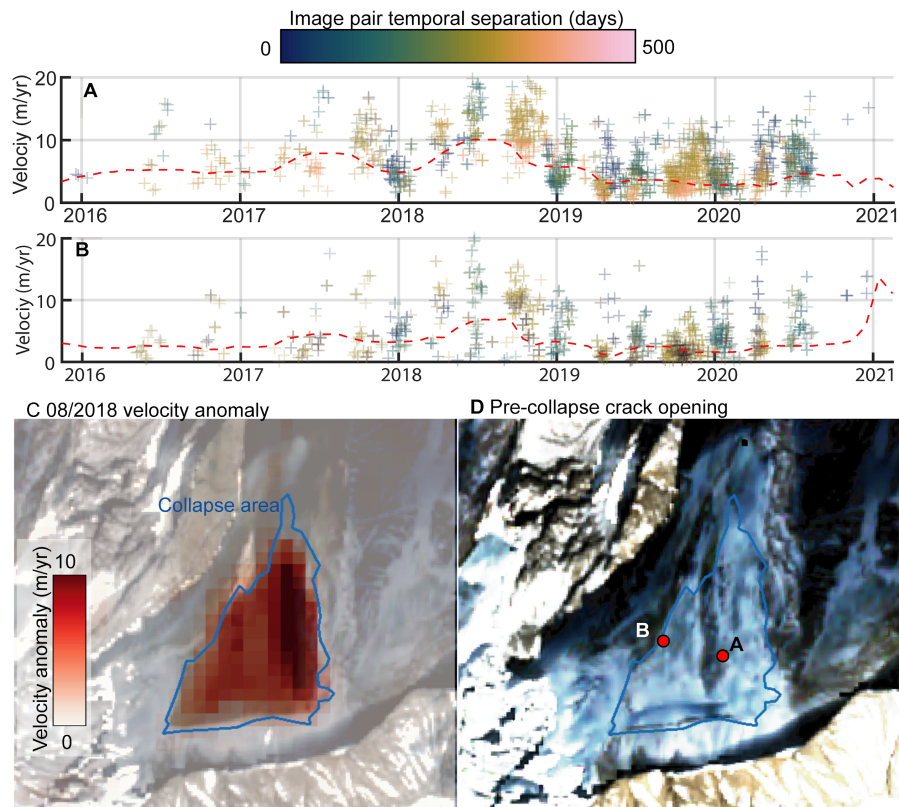


**Fig. S4. Satellite-derived analysis of precursory motion.** (A,B) Time series of slope movement; the red line is the monthly mean velocity (see (D) for locations). (C) August 2018 velocity anomaly (08/2018 velocity minus the 2015-2021 median monthly velocity), highlighting the rapid slip in the collapse area. (D) The growing crack in a 01/31/2021 Sentinel-2 image.

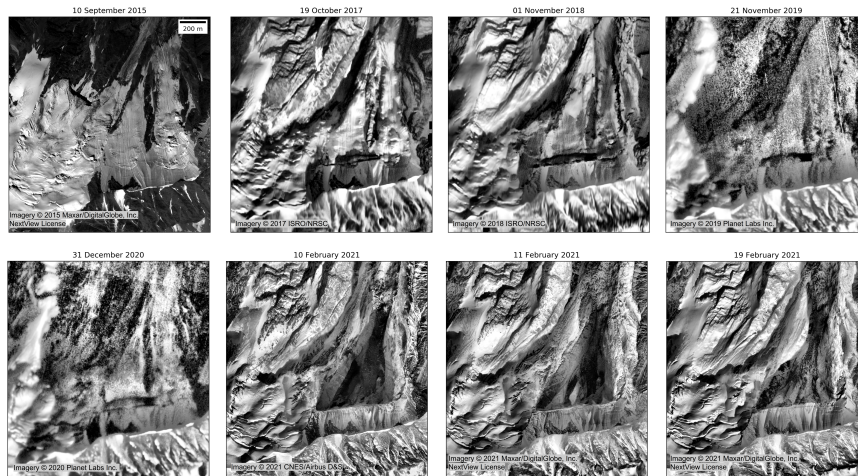


**Fig. S5. High-resolution orthoimages over source area.** Image sequence includes Maxar/DigitalGlobe WorldView-1/2 (PAN, 0.5 m), ISRO/NRSC CartoSat-1 (PAN, 2.5 m), Planet Dove Classic (NIR, ~3-4 m) and CNES/Airbus Pleiades-HR (PAN, 0.5 m) imagery. See Table S2 for more details. All images except September 10, 2015 were enhanced using a Contrast Limited Adaptive Histogram Equalisation (CLAHE) algorithm implemented in the scikit-image package v0.17.1 (105; clip limit 0.05, kernel size of 500 px for <1 m GSD imagery, 125 px for others) to bring out detail over both light (e.g., ice/snow) and dark (e.g., exposed rock) surfaces. The large fracture associated with the February 7, 2021 event is apparent in the October 19, 2017 image, with increased width in the November 1, 2018 image. Limited expansion is observed in subsequent images. The 2021 images show stratigraphy exposed in the west wall of the scar, and deposits from small rockfall events following the large February 7, 2021 collapse. These orthoimages were derived from Level-1B imagery that is © Maxar/Digitalglobe, Inc. (NGA NextView License), ISRO/NRSC, Planet Labs, Inc., and CNES/Airbus DS. Pre-event images were orthorectified using the September 2015 DEM Composite (60), post-event images were orthorectified using the February 2021 DEM Composite (61).

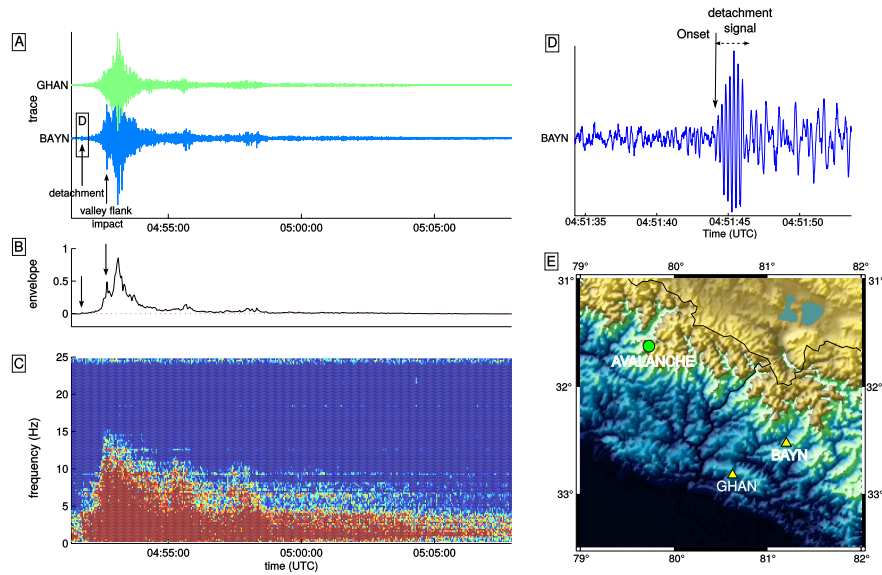


**Fig. S6. Seismic signals generated by the Chamoli avalanche and subsequent debris flow (A), recorded at stations BAYN and GHAN (located on E). The signal envelope and the spectrogram are shown in (B) and (C). (D) shows an enlargement of (A) for the onset of the seismic signal, highlighting the impulsive signal attributed to the detachment of the rockslide. Arrows on (A) and (B) indicate the times of the detachment signal and impacts on the northeastern flank of the valley. (E) shows locations of stations BAYN and GHAN relative to the avalanche.**

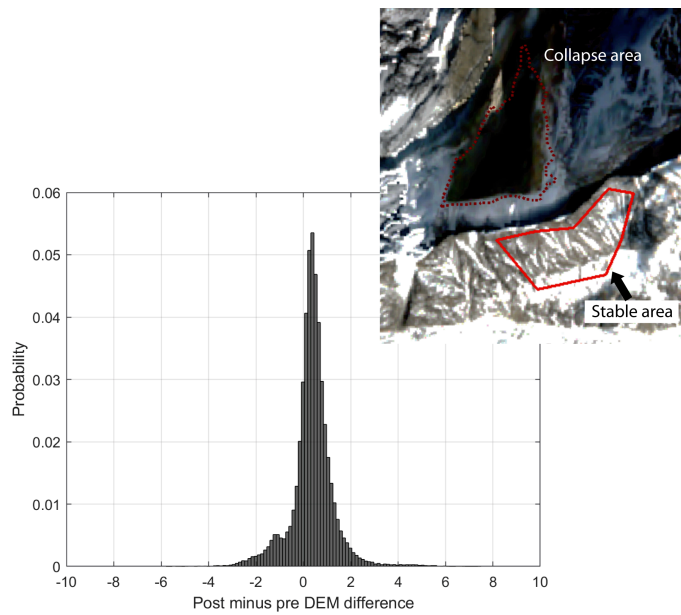


**Fig. S7. Histogram of stable bedrock DEM differences.** Snow cover was higher in the post-event DEM, thus the peak is not centred on zero.



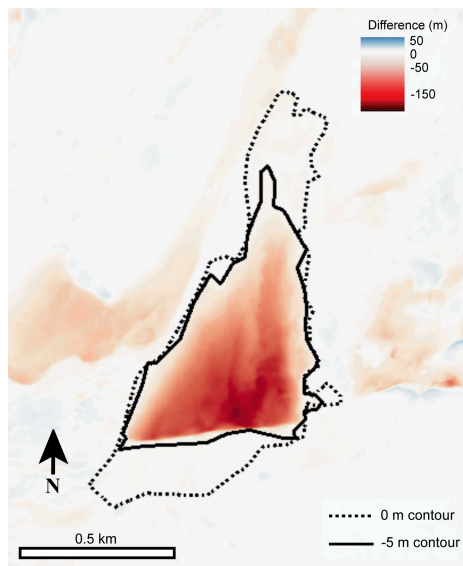


**Fig. S8. Uncertainty in lateral collapse extent.**

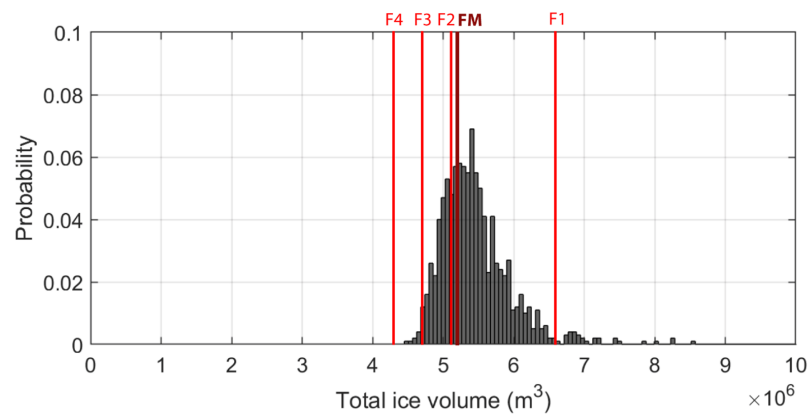


**Fig S9. Ice volume calculation using five different methods.** Methods include ice velocity inversion (black histogram) and Farinotti et al. (118) methods 1-4 (labelled F1-F4). The mean of all four Farinotti estimates is labelled FM.

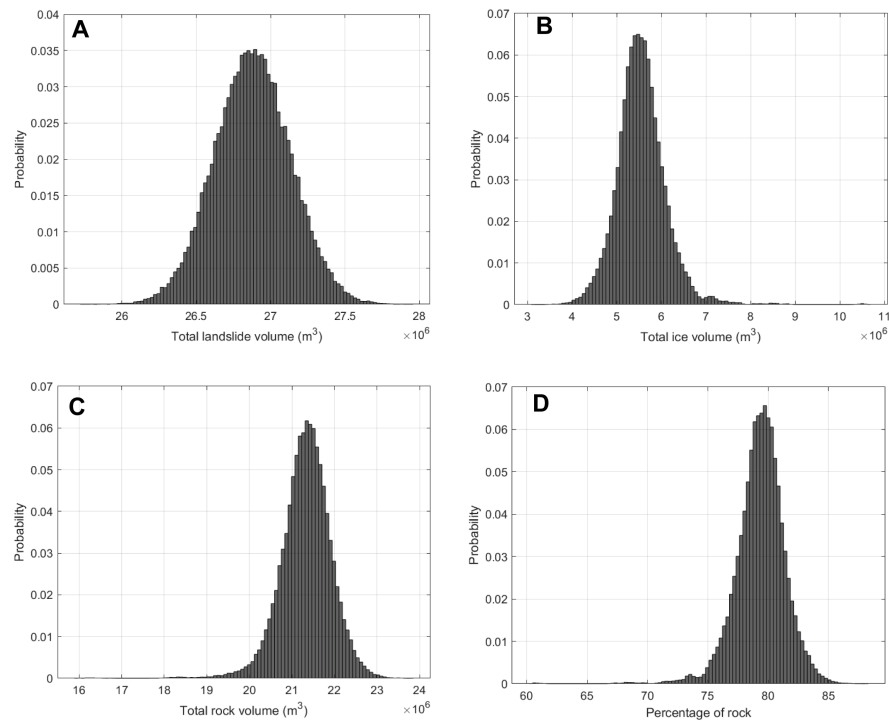


**Fig. S10. Volume of different components.** (A) Total collapse volume, (B) total ice volume, (C) total rock volume, and (D) percentage of rock.

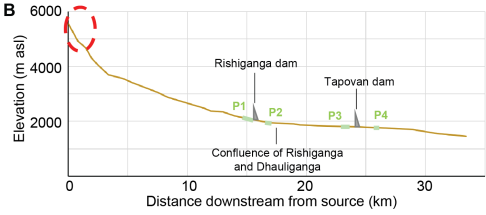
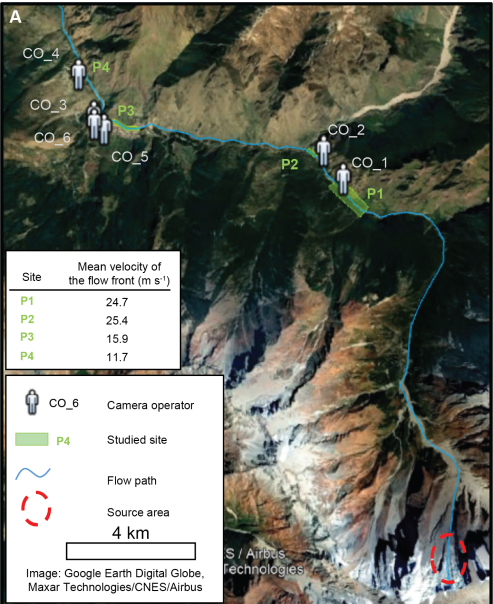


**Fig. S11. Four sites used to estimate mean flow front velocity and discharge along the flow path and approximate location of the six camera operators.**

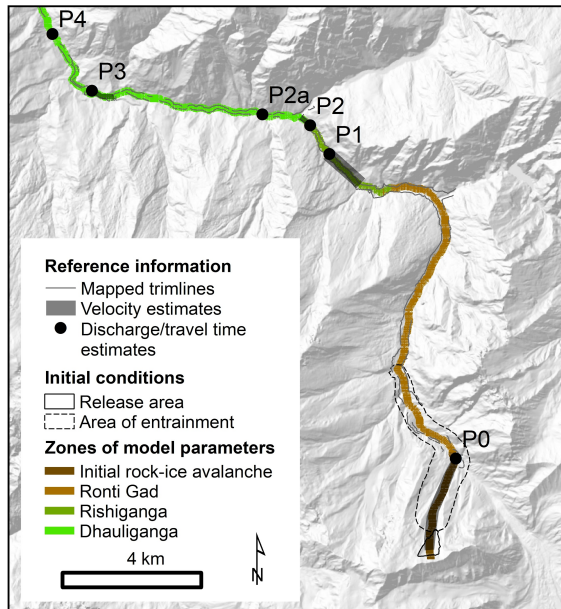


**Fig. S12. Reference information, initial conditions and zones of model parameters used in the numerical simulations.**

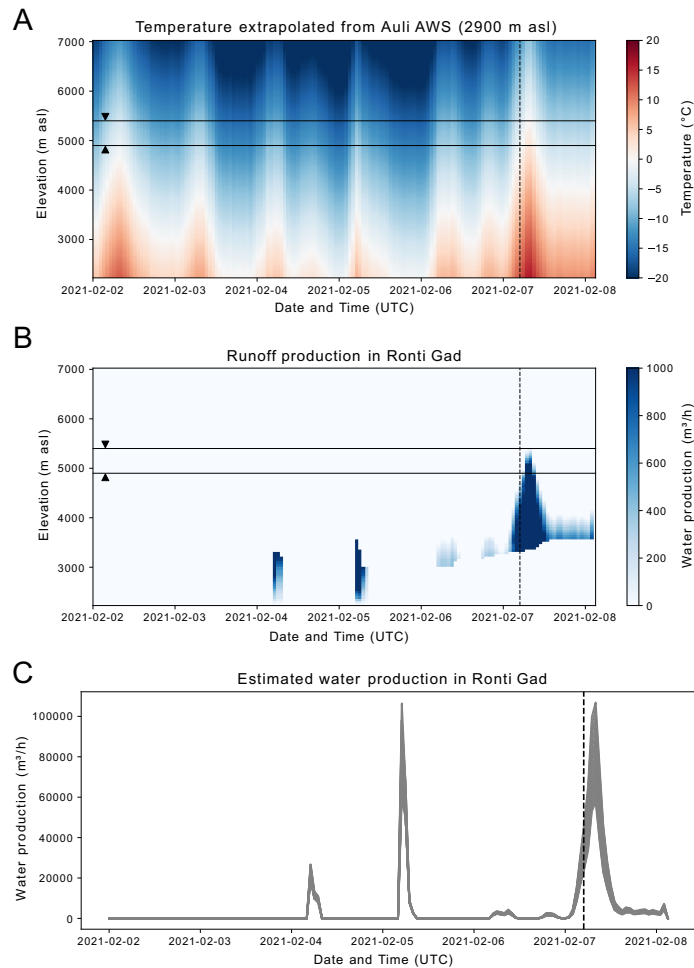


**Fig. S13: Results from water production modeling.** (A) Temperatures extrapolated from the automated weather station (AWS) at Auli (2900 m asl, 30.5283°N, 79.5619E°) using a lapse rate of  $-5^{\circ}\text{C km}^{-1}$  (median lapse rate of seven days prior to the event). (B) Hourly water production estimated by summing rain and snowmelt (degree day factor of  $6 \text{ mm } ^{\circ}\text{C}^{-1} \text{ d}^{-1}$ ). (C) Cumulative water production at all elevations in Ronti Gad modeled with lapse rates ranging from  $-4^{\circ}\text{C km}^{-1}$  to  $-6^{\circ}\text{C km}^{-1}$ . The triangles indicate the upper (▼) and lower (▲) boundary of the failure.

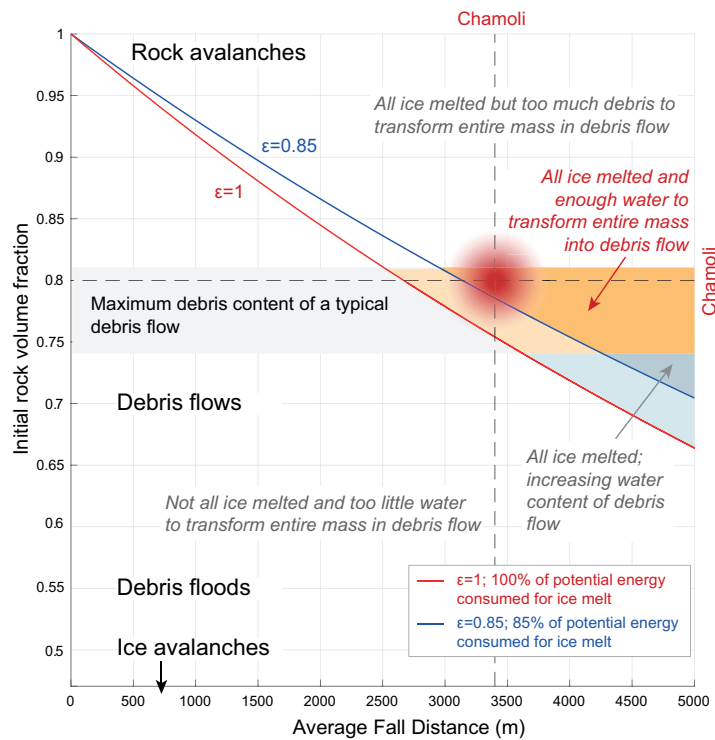


**Fig. S14.** Rock volume fraction that would be able to melt all ice during fall as a function of average fall distance. The vertical dashed line at 3400 m represents the mean fall distance between the site of the initial detachment and the Rishiganga hydropower project. The vertical dashed line indicates the initial rock volume fraction of the detachment of about 0.8. The Chamoli rock and ice avalanche had a combination of rock-ice fraction and fall distance that enabled most ice to be melted and to transform into a debris flow (orange area). For a significantly higher rock fraction (depending on fall distance), not the entire mass can transform into a debris flow (endmember: rock avalanche), for a significantly lower rock fraction not enough water is melted for this transformation (endmember: ice avalanche).

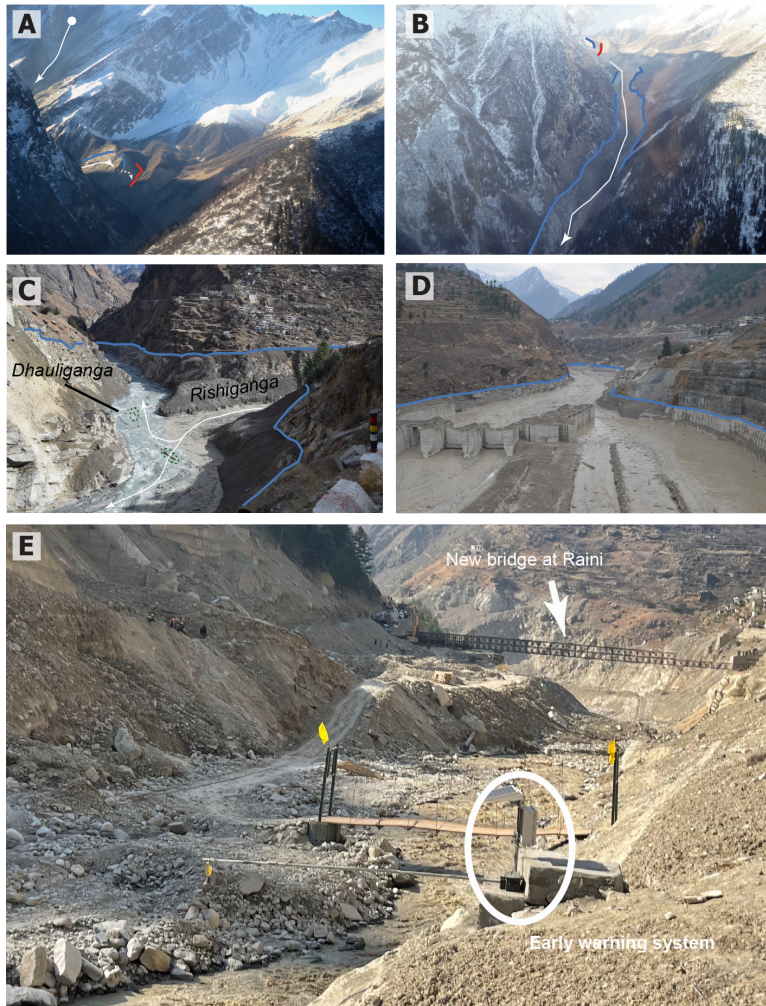


**Fig. S15. Ground-level and helicopter photographs by Amit Kumar/Wadi and M. Farooq Azam.** (A) View up Ronti Gad at the landslide source and upper flow path. Blue and red lines are the mass flow trimlines and splash zones identified in Fig 2. (B) View up Ronti Gad showing mass flow trimlines. (C) View upstream to the confluence of Dhauliganga and Rishiganga rivers with many transported trees (circled in green). (D) View upstream of the destroyed Tapovan hydropower project. (E) View of new iron bridge over Rishiganga River (operational since March 5, 2021) and flood EWS (30°29'00.256" N 79°41'46.886" E, 1947 m asl).



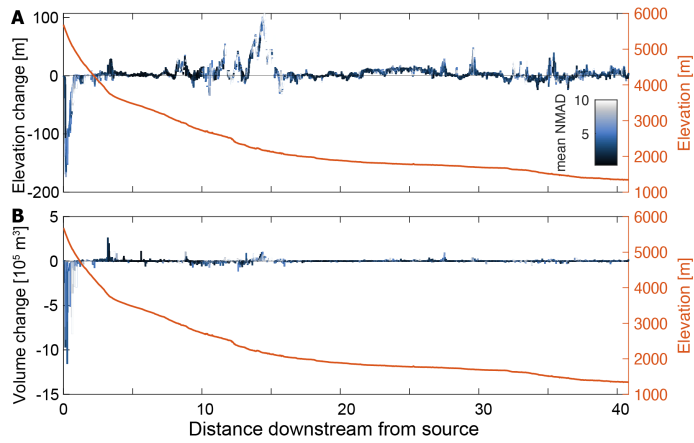


**Fig. S16. Longitudinal profiles of elevation (A) and volume (B) changes from pre-event (2015) and post-event (2021) DEMs.** Changes are calculated within a 500 m-wide swath within the upper 6 km of the flow travel path. For distances beyond this, volume and elevation changes are calculated within 200 and 40 m-wide swaths, respectively. Color ramp shows average normalized median absolute deviation (NMAD, units of meters) of valid elevation difference values within each swath. This metric captures actual elevation change variability and DEM error.

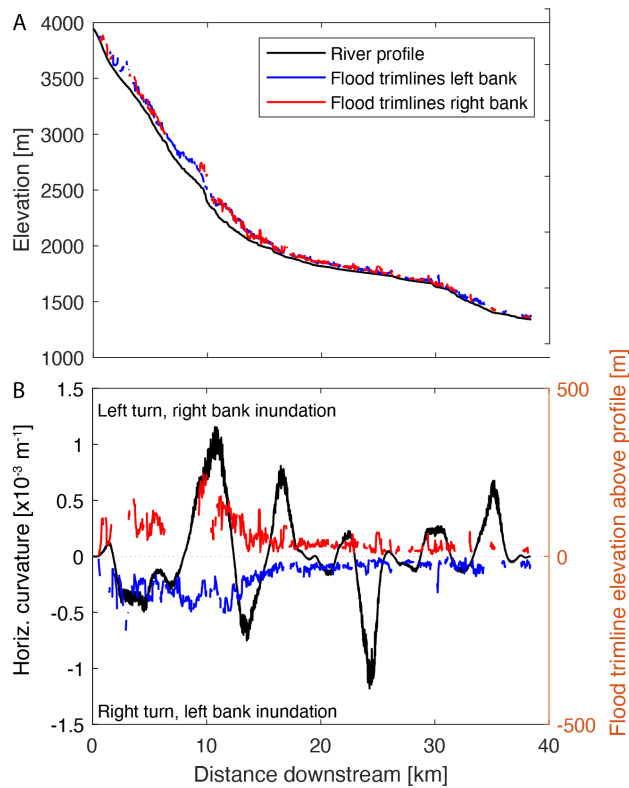


**Fig. S17. Mass flow trimlines mapped from satellite imagery and DEMs.** (A) Elevations of trimlines and river profile. (B) Elevation of trimlines above valley bottom with river planform curvature. River planform curvature at a given point along the river describes the curvature of the approximating circle at that point. Negative and positive values indicate right and left turns, respectively. Higher absolute values denote a sharper planform bend of the river.

1657    **Table S1. Homes of the dead/missing (Source: (124))**

	Indian State/Union Territory & Nepal	No. of people missing/dead
1	Uttarakhand	72
2	Uttar Pradesh	65
3	Jharkhand	13
4	Nepal	11
5	Bihar	9
6	Himachal Pradesh	9
7	Punjab	6
8	West Bengal	6
9	Madhya Pradesh	4
10	Assam	3
11	Delhi	1
12	Odisha	2
13	Haryana	1
14	Jammu and Kashmir	1
15	Unknown (N/A)	1
	<b>TOTAL</b>	<b>204</b>

1658

1659 **Table S2. List of high-resolution satellite images used for geomorphic mapping and**  
1660 **DEM production.**

Pre-event		
Source	Resolution (m)	Date
ESRI BaseMap (RBG)	0.5	September 26, 2014 October 12, 2014 December 21, 2018
SPOT7 (PAN, 4-band MS)	1.5 (6)	October 12, 2014 (tri-stereo) December 24, 2018 (stereo)
WorldView-1 (PAN)	0.5	September 1, 2015 (2) September 10, 2015 September 14, 2015 (2) October 1, 2015 (2) October 5, 2015 (2)
WorldView-2 (PAN, 8-band MS)	0.5	September 28, 2015 (2) September 9, 2018 December 22, 2018
CartoSat-1 (PAN)	2.5	October 19, 2017 (stereo) November 1, 2018 (stereo)
GeoEye-1 (4-band MS)	0.5	April 28, 2019
PlanetScope (4-band MS)	3	November 21, 2019 December 31, 2020 February 6, 2021
During event		
PlanetScope (4-band MS)	3	February 7, 2021
Post-event		
PlanetScope (4-band MS)	3	February 8, 2021
WorldView-1 (PAN)	0.5	February 9, 2021 (mostly cloudy)
Pleiades-HR (PAN, 4-band MS)	0.5 (2.0)	February 9, 2021 February 10, 2021 (stereo)
SkySat-C (PAN, 4-band MS)	0.5-0.7	February 9, 2021 (stereo) February 10, 2021 February 19, 2021
GeoEye-1 (PAN, 4-band MS)	0.5 (2.0)	February 10, 2021 (2)
WorldView-3 (PAN, 8-band MS)	0.3 (1.2)	February 10, 2021
WorldView-2 (PAN, 8-band MS)	0.5 (2.0)	February 11, 2021 (2) February 19, 2021

**Table S3. Characteristics of the avalanche seismic signal at the 2 stations GHAN and BAYN**

	Distance to the source (km)	Arrival time of the first wave (UTC)	Duration (s)
GHAN	159.3	04:51:38.8	855
BAYN	174.3	04:51:43.8	895.8

1664 **Table S4. Videos analyzed in detail.**

Name	Author (channel)	Approx. location of camera operator*	Description	Site ID	Use in the study	Source
Dhauliganga 4*70 MW Cofferdam collapse in Uttarakhand Chamoli... Prayers for Uttarakhand	Electricity Market In India	CO_1	Onset of flow front upstream the Raini dam	P1	Flow velocity estimate	<a href="https://www.youtube.com/watch?v=96n0pxNnQp4">https://www.youtube.com/watch?v=96n0pxNnQp4</a>
TRAVEL ADVISORY: Flash Floods In Uttarakhand (01:06-02:20)	Tripoto	CO_2	Onset of the flow in Raini village	P2	Flow velocity estimate	<a href="https://www.youtube.com/watch?v=mFrKVfv0tyY">https://www.youtube.com/watch?v=mFrKVfv0tyY</a>
VID-20210207-WA0003 (1).mp4	Not known	CO_3	Onset of the flow front in Tapovan (upstream the dam)	P3	Flow velocity estimate	Video sent by Kavita Upadhyay
TRAVEL ADVISORY: Flash Floods In Uttarakhand (00:00-00:22)	Tripoto	CO_4	Onset of the flow front downstream the Tapovan dam	P4	Flow velocity estimate	<a href="https://www.youtube.com/watch?v=mFrKVfv0tyY">https://www.youtube.com/watch?v=mFrKVfv0tyY</a>
???	Kamlesh Maikhuri	CO_5	Live FB stream (since removed); onset of flow front in Tapovan	P3	Timing of flow front arrival to Tapovan	Video provided and verbal permission of the author given to Kavita Upadhyay
Tapovan-one.mp4	Omprakash Thapliyal	CO_6	Onset of flow front in Tapovan	P3	Timing of flow front arrival to Tapovan	Personal communication with the author (by Kavita Upadhyay)

1665

**Table S5. Characteristics of the flow front at four studied sites.**

Site ID	Downstream location from source area	$\Delta d$ [m]	$\Delta t$ [s]	$v$ [m s <sup>-1</sup> ]	$A^*$ [m <sup>2</sup> ]	$Q^{**}$ [m <sup>3</sup> s <sup>-1</sup> ]	$T$ [hh:mm] (UTC+5:30)
P1	14.3 km	1260	51	24.7	318.75 to 525.50	8,191 to 14,199	10:30-10:32 <sup>#</sup>
P2	16.7 km	330	13	25.3	281.25 to 487.50	7,116 to 12,334	10:31-10:33 <sup>#</sup>
P3	23.6 km	540	34	15.9	300.00 to 528.00	4,770 to 8,411	10:38-10:40
P4	25.7 km	70	6	11.7	243.75 to 422.50	2,852 to 4,943	10:41-10:42 <sup>#</sup>

\*Notes: Approximated from idealized trapezoidal cross-profile with different slope steepness and flow depth.

\*\*  $Q$  calculated as the product of mean velocity and cross-profile area ( $Q = v \cdot A$ ).

<sup>#</sup> Values calculated from known onset of the flow front at Tapovan dam (site P3) and estimated mean flow-front velocities.